Materials & Design 234 (2023) 112323

Contents lists available at ScienceDirect

Materials & Design

journal homepage: www.elsevier.com/locate/matdes

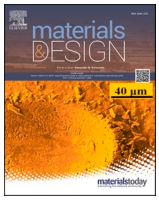

Design of high-strength martensitic steels by novel mixed-metal nanoprecipitates for high toughness and suppressed hydrogen embrittlement

Masoud Moshtaghi [a,*], Emad Maawad [b], Artenis Bendo [c], Andreas Krause [d], Juraj Todt [e,f], Jozef Keckes [e,f], Mahdieh Safyari [g,h]

[a] Chair of General and Analytical Chemistry, University of Leoben, Franz Josef-Straße 18, 8700 Leoben, Austria
[b] Helmholtz-Zentrum Hereon, Institute of Materials Physics, Max-Planck-Str. 1, Geesthacht, Germany
[c] Department of Materials, The University of Manchester, Oxford Road, Manchester M13 9PL, United Kingdom
[d] Department of Materials Science and Applied Mathematics, Malmö University, SE-211 19 Malmö, Sweden
[e] Department of Materials Science, Montanuniversität Leoben, Franz-Josef-Strasse 18, 8700 Leoben, Austria
[f] Erich Schmid Institute for Materials Science, Austrian Academy of Sciences, Leoben, Austria
[g] LKR Light Metals Technologies Ranshofen, Austrian Institute of Technology, 5282 Ranshofen, Austria
[h] Institute for Materials Research, Tohoku University, 2-1-1 Katahira, Aoba-ku, Sendai 980-8577, Japan

ARTICLE INFO

Keywords:
Hydrogen embrittlement
Martensitic steels
Atome probe tomography
Experimental-simulations synergy
High-energy synchrotron X-ray diffraction
Hydrogen mapping

ABSTRACT

To obtain a fundamental understanding of mechanisms of hydrogen embrittlement (HE) and its prevention in advanced high-strength steels containing novel nanoscale mixed-metal precipitates, it is necessary to study local microstructure, H trapping, and crack path with new multiscale experimental and simulation approach. Spatially resolved hydrogen mapping via SKPFM is used together with investigation of the crack path using high-resolution EBSD and HMPT, and global trapping behavior of the alloys by TDS. These results are combined with newly introduced method to elucidate real-time distribution of hydrogen in the alloy using high-energy synchrotron X-ray diffraction (HES-XRD). Mixed-metal precipitates improves HE resistance of the alloy, due to nature of the trapping sites, e.g. irreversible H-trapping by carbon vacancies inside novel nanoprecipitates and high total length of PAGBs. This is because of lower possibility of build-up of critical local hydrogen content at PAGBs for intergranular hydrogen-assisted cracking due to hydrogen-enhanced decohesion mechanism. Less weakly trapped hydrogen also reduces frequency of dislocation activation and enhanced dislocation slip in {0 1 1} slip plane due to hydrogen-enhanced localized plasticity in regions with affinity for transgranular hydrogen-assisted cracking at lower local hydrogen content. Direct evidence of carbon vacancies in novel nanoprecipitates is observed for the first time via HAADF-STEM.

1. Introduction

Controlling microstructure to include precipitates in advanced high-strength steels (AHSS) is a technique commonly used to improve the hydrogen embrittlement (HE) behavior of steels. The addition of precipitate-forming elements, namely Ti, Mo, V, and Nb, leads to an improvement in the strength due to precipitation hardening as well as the HE behavior of the AHSSs [1–4]. Vanadium has a special effect on steels due to its increased solubility in austenite at high temperatures, which leads to dissolution during heating, resulting in the formation of fine nanoprecipitates. Nb-containing precipitates have a higher precipitation temperature than V-containing ones [5–7], suggesting that NbC can more efficiently prevent recrystallization of the austenite matrix via pinning the migrating prior austenite grain boundaries (PAGBs) [8]. In addition, Nb has a similar electronic structure to V, which leads to competition with V in precipitate formation. Therefore, the simultaneous addition of Nb and V may have two beneficial effects on material properties: dispersion of fine precipitates and control of static recrystallization of prior austenite grain (PAGs) during hot rolling. This suggests that the V + Nb micro alloy may be used simultaneously as precipitate-forming elements.

It is known that microstructural control can affect the HE behavior of

* Corresponding author.
E-mail address: masoud.moshtaghi@unileoben.ac.at (M. Moshtaghi).

https://doi.org/10.1016/j.matdes.2023.112323
Received 28 July 2023; Received in revised form 2 September 2023; Accepted 12 September 2023
Available online 14 September 2023

steels by influencing the trapping states and migration patterns of hydrogen. The trapping sites of hydrogen in an alloy are considered to be one of the key factors affecting the HE behavior of the steels [9,10]. Traps in an alloy are generally categorized into reversible and irreversible traps, based on the calculated binding energy of hydrogen at the specific trap site [9,11,12]. Hydrogen trapped at reversible trap sites is diffusible hydrogen, while hydrogen trapped at irreversible ones are considered non-diffusible hydrogen. The desired mechanism for mitigating HE susceptibility in AHSS is to introduce relatively irreversible hydrogen trap sites to the alloy to minimize the amount of diffusible hydrogen that can reach crack tip or potenital flaws [13–17]. Several studies have been performed to characterize hydrogen-carbide interactions. Lee et al. [18] and Wei et al. [19] showed that some carbides are strong trap sites that can reduce diffusible hydrogen content. However, it was also reported that the trapping behavior of these carbides depends on several parameters such as size, chemical composition, trapping capacity, and coherency [20,21]. The concept of deep traps has been applied to single-metal carbides, leading to the development of nanocarbides in martensitic alloys to suppress HE. The trap capacity of the carbides is ordered as NbC > TiC > VC > Mo_2C, showing that NbC has the highest capacity to trap H [20]. The addition of some of these elements showed significant HE mitigation, however, the mechanical properties are not desirable and there is considerable loss of elongation [17,22,23]. Wei and Tsuzaki [17] reported the shape and size of the precipitates have a decisive influence on the mechanical properties and HE behavior of the alloys. The disk-shaped precipitates form in a relatively coherent or semicoherent state, while at high tempering temperatures the incoherent precipitates form in a spherical shape. It has been already reported [21,24] that the strengthening effect of the finer nanoprecipitates is due to the generation of an antiphase boundary and leads to improved strength and toughness compared to the incoherent nanoprecipitates. The addition of combined Nb and V can result in finer precipitates in a similar tempering temperature with single-metal carbides and can inhibit recrystallization of the austenite matrix more efficiently via pinning the migrating PAGBs. The former leads to an increase in strength and ductility due to the beneficial effect of nanoprecipitates with the generation of antiphase boundaries [21,24] and the latter leads to a finer grain size and a better combination of strength and ductility due to the Hall-Petch effect [25]. This suggests that V + Nb microalloying can contribute to improving alloy strength and ductility. Despite several studies conducted on the effect of single-metal carbide-forming elements on the HE behavior of AHSS, the effect of nano-sized (Nb,V)C mixed-metal precipitates and their hydrogen trapping nature in high-strength martensitic steels on HE behavior and mechanical properties of the alloy has not yet been investigated.

To investigate the effects of mixed metal precipitates on the HE behavior and mechanical properties of AHSS, the V + Nb microalloyed martensitic steel is compared with the basic martensitic Fe-C steel. This leads to unveiling the effects of the mixed metal precipitates on the HE behavior and mechanical properties of the martensitic steel. In the present study, combined advanced, multiscale, comprehensive experimental and simulation approach was used to characterize the microstructure of AHSS and hydrogen-precipitate interaction. These techniques include atomic and sub-atomic characterizations such as atom probe tomography (APT), scanning transmission electron microscopy (STEM), in situ scanning Kelvin probe force microscopy (SKPFM), and hydrogen microprint technique (HMPT) in combination with atomistic simulation through density functional theory (DFT). In addition, thermal desorption spectroscopy (TDS), electrochemical hydrogen permeation measurements, and high-resolution electron backscatter diffraction (EBSD) were used for crack path studies. A novel method for measuring hydrogen distribution in the alloy using high-energy synchrotron X-ray diffraction was introduced and used for the first time. The combination of these techniques allows us to perform multiscale hydrogen mapping and understand the hydrogen distribution in the alloy, from the macroscale to the nanoscale. This multiscale experimental and simulation approach and the obtained results are used to clarify the mechanism of hydrogen-assisted cracking, the crystallographic features of H-assisted fracture, and its prevention in martensitic steels with and without nano-sized (Nb,V)C mixed metal precipitates.

2. Experimental procedures

2.1. Materials

The contents of precipitate-forming elements were chosen considering preliminary density functional theory (DFT) calculations of the solution energies of hydrogen at the octahedral and tetrahedral interstitial sites of the (Nb,V)C mixed-metal precipitate with respect to different ratios of Nb and V (See appendix 1). The results indicate that the hydrogen trapping at the mixed-metal precipitates is most favorable at a composition of $Nb_{0.25}V_{0.75}C$. It was also shown that niobium defects in VC minimize the surface energy when they are located at the carbide surface [26]. The VC_x precipitates are supposed to contain Nb defects, since the observed increased lattice parameter [27,28]. Therefore, for martensitic steel containing (Nb,V)C mixed-metal precipitates, the composition mentioned in Table 1 was considered. The composition of the formed mixed-metal precipitates with the calculated chemical composition will be measured experimentally by APT. Two alloys were produced in an induction melting system under Ar atmosphere. The obtained cast bars were subsequently hot rolled and heat treated at 1250 °C for 2 h to allow them to austenitize. They were then immediately quenched in ice brine followed by sub-zero cooling in liquid nitrogen. This was followed by a tempering treatment at 740 °C for 20 min. The tempering treatment was chosen based on previous studies about its effects on the shape and size of the precipitates [29,30].

2.2. Electrochemical charging

Electrochemical hydrogen charging of the samples was performed. A cylindrical Pt mesh electrode was used as anode and the sample as cathode with a cathodic current density of 10 mA in an aqueous 3.5% NaCl solution with 1 g/l thiourea was used to avoid recombination of hydrogen. After electrochemical hydrogen charging, liquid nitrogen was used for cooling the specimens to avoid the effusion of hydrogen before analyzing the specimens.

2.3. In-situ slow-strain rate testing (SSRT)

Before starting the SSRT, the specimens were precharged in the same solution, current density, and charging time mentioned in section 2.2. The SSRT tests with in situ H charging were carried out at the strain rate of 3.4×10^{-6} s^{-1}. The dimensions of the gauge part of the flat tensile specimen are $12.0 \times 5.0 \times 2.0$ mm^3. As a reference test, an SSRT with a similar strain rate was done in the air. To ensure adequate repeatability, tests were performed three times per condition and representative results were reported.

2.4. SEM, FIB lift-out and high-resolution EBSD

Microstructures were characterized using a Zeiss GeminiSEM 560 field emission scanning electron microscope (FE-SEM) in conjunction with an Oxford EBSD system and focused ion beam (FIB). All samples were prepared by grinding, followed by electropolishing. The ion slicing technique (Hitachi IM4000 +) was used with parameters of 15° tilting

Table 1
The chemical composition (wt %) of the alloys under study.

Alloy	C	Nb	V	Fe
Fe-C	0.081	–	–	Balance
Fe-C-Nb-V	0.091	0.07	0.28	Balance

angle and 6 kV voltage. More details about the ion slicing procedure can be found elsewhere [31].

2.5. Scanning transmission electron microscopy (STEM)

The microstructures of the specimens were observed using an atomic resolution electron microscope (JEOL-JEM -ARM200F) equipped with spherical aberration correctors to perform typical HAADF-STEM and bright field TEM. For this purpose, the samples were first mechanically ground and then electropolished at 15–20 V and − 20 °C using the twin-jet polishing method and a solution (20% perchloric acid + 80% methanol) as electrolyte.

2.6. Atom probe tomography

To investigate matrix and precipitate composition, atom probe tomography (APT) specimens of the alloy were prepared using a FEI Helios NanoLab 600i SEM /focused ion beam (FIB) dual-beam instrument on commercially available silicon micro-tip coupons. The samples were milled with a 30 kV Ga^+ beam, with an additional cleaning step (5 kV and 40 pA) to remove damaged regions induced by the Ga^+ ions. A site-specific preparation was performed for APT characterization of the mixed-metal precipitates. 20% nitric acid in methanol and 2% perchloric acid in 2-butoxyethanol were used as the solutions for two-step electropolishing. Tip radii were measured by SEM at around 450 nm. FIB milling was used for shape the tip to the desired shape. FIB milling was repeated when the precipitate position was monitored by transmission Kikuchi diffraction (TKD). The more experimental details of the APT measurements were mentioned in our previous work [32].

2.7. Measurement of hydrogen distribution using high-energy synchrotron X-ray diffraction

For a qualitative assessment of the H depth distribution due to H charging, samples of approx. 3 × 10 × 10 mm in size were prepared by careful mechanical grinding with corundum abrasive and polishing in a diamond suspension. Directly before the measurement, the samples were electrochemically H-charged from all sides for one hour in a 3.5 % NaCl solution with 1 g/l CH_4N_2S (thiourea), using a current density of 10 mA/cm^2. Charging took place in a chemical laboratory in close proximity to the high-energy synchrotron X-ray diffraction (HES-XRD) experimental station at beamline P07b of the synchrotron PETRA III, operated by Helmholtz Zentrum Hereon at Deutsches Elektronen Synchrotron (DESY) in Hamburg, Germany. A reference state of each sample was measured before the start of H charging, to be able to account for any inhomogeneities in lattice parameter depth distribution due to sample preparation and the initial microstructural state. The measurements were performed in cross-sectional transmission geometry, with a Perkin Elmer 2-dimensional (2D) detector placed approx. 1.3 m downstream of the sample. The size of the X-ray beam was set to 10 × 500 μm (depth × width) and the photon energy was set to 87.1 keV. The exact detector geometry was calibrated with a LaB_6 standard powder using the calibration routines provided by the pyFAI software package. The same software was then also employed to integrate the 2D diffraction patterns within 40° azimuthally around the directions perpendicular to the sample surface. Employing Bragg's law, the lattice parameter was calculated as an average value from the first 5 diffraction rings 110, 200, 211, 220 and 310, considering that the chosen direction is comparatively insensitive to changes in the residual stress state, since only the effect of Poisson contraction would be visible.

2.8. Hydrogen electrochemical permeation (EP) experiments

Electrochemical permeation experiments were performed using D-S cell [33]. The electrolyte in the galvanostatically charging cell was a 3.5% NaCl solution with 1 g/l CH_4N_2S (thiourea) and a current density of 1 mA cm^{-2}, and the electrolyte for the oxidation cell of a 0.1 mol/l NaOH solution was used. The experimental conditions are listed in Table 2, and the other details of the technique can be found elsewhere [34]. The effective diffusion coefficient (D_{eff}), the apparent hydrogen solubility (c_{app}) of the sample material for hydrogen, the permeation coefficient (permeability, Φ), and density of trap sites (N_T) were calculated by the following equations:

$$D_{eff} = \frac{L^2}{6 \cdot t_{lag}} \tag{1}$$

$$c_{app} = \frac{j_\infty L}{D_{\text{eff}}} \tag{2}$$

$$\Phi = c_{app} \cdot D_{\text{eff}} \tag{3}$$

$$N_T = \frac{c_{app}}{3}\left(\frac{D_L}{D_{\text{eff}}} - 1\right) N_A \tag{4}$$

where t_{lag} is the time required for reaching the oxidation current to 0.63 steady-state value, L is the sample thickness, j_∞ is steady-state hydrogen flux per area, D_L is lattice diffusion coefficient and N_A is Avogadro constant.

2.9. Thermal desorption spectroscopy

Thermal desorption spectroscopy (TDS) was performed using an instrument equipped with a quadrupole mass spectrometer. The samples under study were charged with a 5% NaCl solution containing 1 g/l CH_4N_2S at 23 °C with a current density of 10 mA/cm^2 for one hour. After charging with hydrogen, liquid nitrogen was used to prevent escape of H from specimen. The samples with the thickness of 0.5 mm were then rinsed with acetone and weighed in the dry state. The samples were then heated at a rate of 300 K.h^{-1}. The calibration gas was a mixture of $N_2 + 5$ % H_2. The linear regression of the slope of $d(ln\left(\frac{\varphi}{T_m^2}\right))$ as a function of $d(\frac{1}{T_m})$ was used to calculate the desorption energy (E_d) of the H traps in different heating rates [24,35]:

$$\frac{d\left(ln\left(\frac{\varphi}{T_m^2}\right)\right)}{d\left(\frac{1}{T_m}\right)} = -\frac{E_d}{R} \tag{5}$$

where T_m, φ, E_d, and R *are* the center of the peak, the heating rate, desorption energy and the gas constant, respectively.

2.10. Hydrogen microprint technique (HMPT)

To characterize the local sites of hydrogen accumulation, a hydrogen mapping technique, HMPT was used. The tensile-tested sample with polished surface was electrochemically charged and subjected to HMPT mapping. The AgBr solution was used, followed by applying formalin to harden the gelatin layer and $Na_2S_2O_3$ aqueous solution. More details of the HMPT can be found elsewhere [9,36].

Table 2
Experimental conditions used for electrochemical permeation test.

Electrolyte charging cell	3.5 % NaCl + 1 g/l CH_4N_2S
Electrolyte oxidation cell	0.1 mol/l NaOH
Charging current density	1 mA cm^{-2} (constant)
Oxidation potential	546 mV vs. SHE (constant)
Gas purging	0.2 l/min Ar (purity ≥ 99,999 %)
Counter electrode	Pt
Reference electrodes	Ag/AgCl (sat. KCl)
Temperature	25 ± 0.5 °C
Sample thickness	1 mm
Sample coating	100 nm Pd on exit side
Sample area on charging side	1.348 cm^2
Sample area on oxidation side	1.094 cm^2

2.11. Density function theory (DFT) calculations

The Vienna ab-initio Simulation Package (VASP) plane was utilized to perform wave DFT calculations. Periodic boundary conditions as well as spin polarization were applied. The gradient approximation was used with a correlation functional based on the Perdew-Burke-Ernzhof scheme with a cut-off energy of 520 eV. A Monkhorst-Pack 12 × 12 × 12 k-point mesh on the unit cell was used and adjusted accordingly for larger supercells. Size convergence was checked and found to have a maximum error of 20 meV when using a 3 × 3 × 3 supercell.

Vibrational frequencies have been calculated by keeping the metal and carbon atoms fixed, while hydrogen was perturbed in each direction by 0.015 Å. The zero-point energy (ZPE) was approximated as $ZPE = \frac{1}{2}\sum_i \hbar\nu_i$, where $\hbar$ is the plank constant divided by 2 π and ν are the vibrational frequencies.

2.12. In-situ SKPFM experiment procedure

The scanning kelvin probe force microscopy (SKPFM) measurements were performed under dry nitrogen gas at room temperature using an Agilent 5500 AFM. Hydrogen was introduced into the Fe-C-Nb-V samples via hydrogen charging by a 5% NaCl solution containing 1 g/l CH_4N_2S at 23 °C with a current density of 10 mA/cm^2 for 24 h, and then a thin Pd layer was physically vapor deposited on the surface as a detection layer for the hydrogen. Then the sample was transferred to the SKPFM, where the probe was a conductive Pt-coated silicon tip and the tip was vibrated over the surface at different frequencies. Therefore, the tip performance is not stable and often the tips jump due to contamination, resulting in uncalibrated measurements of the potentials with the SKPFM that are not suitable for quantification. However, evaluation of the potential contrast over time provides important information about the varying rates of hydrogen desorption from the traps.

3. Results

3.1. Crystal orientation, phase analysis and grain growth inhibition

Figs. 1 and 2 show the EBSD results obtained for Fe-C and Fe-C-Nb-V alloys, respectively. The inverse pole figure (IPF) maps show that after the addition of (Nb,V)C mixed-metal precipitates, the martensite packets, blocks, and the prior austenite grain boundaries (PAGBs), as well as the overall microstructure, become more homogeneous. The colors in the IPF map show the orientations parallel to the normal direction of the section under consideration based on the stereographic triangle under the EBSD orientation map. The intensity of the texture decreased with the addition of (Nb,V)C mixed-metal precipitates, meaning that the Fe-C alloy showed a strong texture and the Fe-C-Nb-V alloy showed a weaker texture. In fact, the intensity of the {1 1 1} texture can be reduced with the addition of (Nb,V)C mixed-metal precipitates. The grains in the Fe-C alloy are free to grow in the {1 1 1} direction, and with (Nb,V)C mixed metal precipitates this growth can be confined. The inhibition of grain growth of the prior austenite at high temperatures [37] via the (Nb,V)C mixed-metal precipitates leads to a finer martensite microstructure. The high-temperature stability of the nanoprecipitates leads to effective grain growth inhibition [37,38]. Grain growth inhibition affects the size of the prior austenite grain (PAG) and the martensite microstructure.

Fig. 1d and 2d show the phase maps of the Fe-C and Fe-C-Nb-V alloys, respectively. The results show that the total carbide content is higher in the Fe-C-Nb-V alloy than in the Fe-C alloy. The phase maps also show that the two alloys do not contain retained austenite. However, it is known that when the size of retained austenite phase particles is in the order of few nanometers, the Kikuchi pattern of the retained austenite can overlap with the pattern of the austenite matrix, so that the confidence index (CI) of the austenite block is very low [39]. Therefore, the nano-sized retained austenite cannot be detected by EBSD measurement. It has already been reported that retained austenite affects the hydrogen trapping capacity and hydrogen embrittlement behavior of high-strength martensitic steel [40]. HES-XRD is a powerful tool for in-situ characterization of structural steels considering the effects of nanophases [41,42]. Thus, HES-XRD is used to detect nanophases as well as a novel method to detect the hydrogen distribution profile in the martensitic microstructure.

3.2. Characterization of particles

Fig. 3 shows the TEM, scanning TEM (STEM), high-angle annular dark-field STEM (HAADF-STEM) micrographs and atom probe

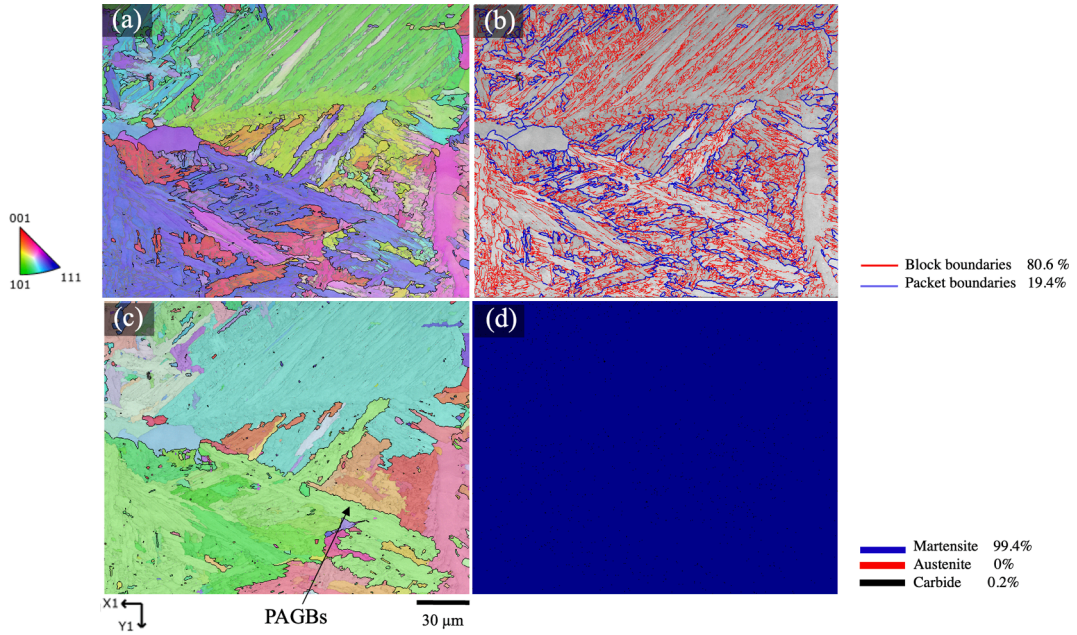

Fig. 1. (a) inverse pole figure (IPF) and (b) boundary map of martensitic structure, (c) prior austenite microstructure obtained by Kurdjumov-Sachs relationship between martensite and austenite, and (d) phase map of Fe-C alloy.

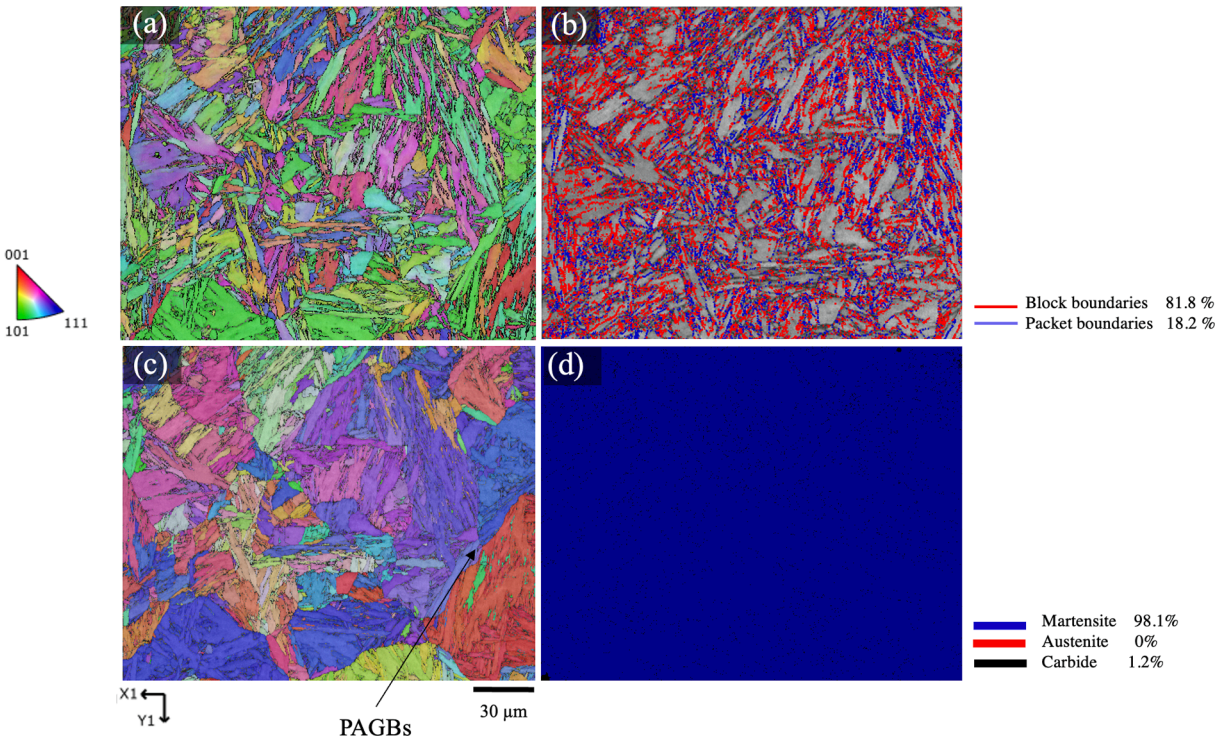

Fig. 2. (a) inverse pole figure and (b) boundary map of martensitic structure, (c) prior austenite microstructure obtained by Kurdjumov-Sachs relationship between martensite and austenite, (d) phase map of Fe-C-Nb-V alloy.

tomography (APT) map reconstruction of the (Nb,V)C mixed metal precipitates. It has already been reported that Nb alters the solidification pathway. Vanadium carbides host large amounts of niobium [27]. The alloy showed the presence of nanosized precipitates, with an average size of 12 nm (Fig. 3a and b). Fig. 3c shows the pattern of diffraction of selected areas (SAD) pattern of Fe-C-Nb-V alloy. This includes the points associated with (Nb,V)C mixed-metal precipitates (as shown by green arrows). From the diffraction, the interplanar spacing of d{hkl}(Nb,V)C corresponds to 2 times the interplanar spacing of the d{1 3 0}Fe matrix. Vanadium and niobium precipitates are isomorphous and have the cubic NaCl lattice B1 [27], and comparable size have been reported in other research [43]. Experiments at high temperatures have established continuous series of solid solutions. Liu et al. [44] explained the progression of mixed-metal (Nb,V)C equilibrium phase as follows: isostructural diffuse atmospheres → Fe-depleted V-Nb clusters → metastable transient phases (Fe,V,Nb)C → (Nb,V)C equilibrium phase. In the formed mixed-metal precipitates with the mentioned nominal composition in Fe-C-Nb-V quaternary alloys, solubility of niobium was observed, where about 25% of vanadium atoms could be replaced by niobium. Fig. 3d-g show HAADF-STEM images of a (Nb,V)C precipitate particle, an inverse fast Fourier transform (IFFT) of it, and the schematic representation of atom positions and the coherent and incoherent interfaces of the precipitates. The lattice parameter of the (Nb,V)C particle with cubic NaCl lattice B1 structure was measured to be 4.364 Å. This is in agreement with the results of a previous study [45]. The IFFT results also showed that there are some misfit dislocations in side interface of the (Nb,V)C mixed-metal precipitates, indicating an incoherent side interface of the (Nb,V)C mixed-metal precipitates. The smooth interface (broad interface) along (1 0 0) is coherent, which has also been reported by other studies [46,47]. The disk-like precipitates with similar interface properties have already been mentioned in recent findings [30,48].

Fig. 3f shows the APT compositional analysis results of the (Nb,V)C mixed-metal precipitates, with gray, blue, orange, and green indicating Fe, C, Nb, and V atoms, respectively. The results also show the 1-D concentration profile of the region of interest in the APT reconstruction microscopy (marked by a red rectangle). The results indicate the presence of carbon at the interface and show that the octahedral sites at the interface (preferred interstitial sites for C or H [48]) are already occupied by carbon. This indicates that there are only a limited number of vacant octahedral sites at the interface that can accommodate hydrogen. Therefore, remarkable hydrogen trapping at the octahedral sites of the interfaces cannot be considered in this alloy. The obtained results also show that the carbon concentration in the carbide is lower than expected for this mixed-metal precipitate than stoichiometric. This carbon deficit can be associated with carbon vacancies, which are also already observed for the carbides [20]. Recent studies suggest that the quantification approach used here is associated with accurate results, especially for carbon content [49,50]. The formation of (Nb,V)C mixed-metal precipitates in steels with carbon vacancies has also been shown previously in another study [26] which agrees with the current results of APT. Fig. 3i shows the atomic resolution HAADF images of the mixed-metal precipitates. The very dark centers as indicated by a blue rectangle in the magnified HAADF-STEM image could be related to carbon vacancies. This means that these are most likely (Nb,V)C mixed-metal precipitates in the alloy with multiple carbon vacancies. A similar method for observing vacancies has already been used in a recent research paper [51].

3.3. *Mechanical properties and fractography*

The stress–strain curves of the alloys with and without electrochemical hydrogen charging are shown in Fig. 4. It can be seen that the mechanical properties of the alloys tested with hydrogen were changed compared to the specimens tested in air. The yield strength and ultimate tensile strength of the specimens tested with and without hydrogen did not change significantly and the results are comparable. The elongations of the H-charged specimens were reduced compared to the uncharged condition, indicating that hydrogen embrittlement in the alloys occurs after the absorption of hydrogen by the electrochemical hydrogen charging [24,31,52,53]. This elongation loss for the H-charged Fe-C-Nb-

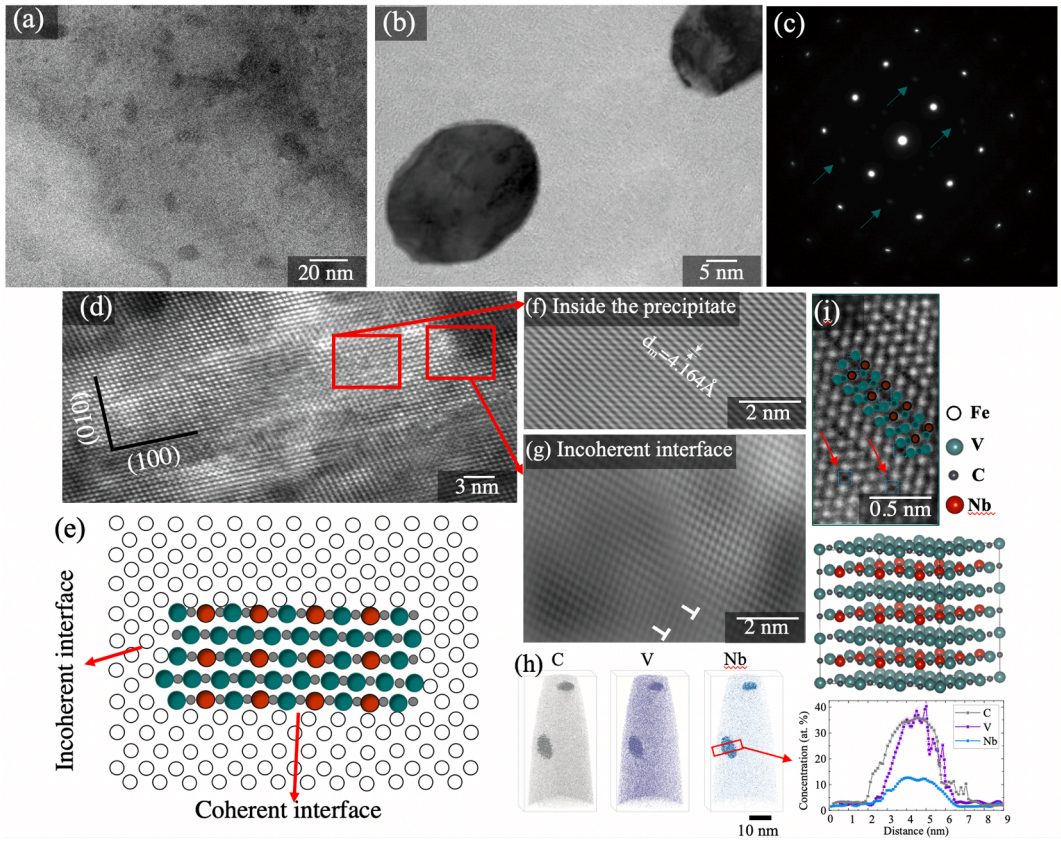

Fig. 3. (a) STEM micrograph of the Fe-C-Nb-V alloy, indicating the distribution and size of (Nb,V)C carbides. (b) Magnified high-resolution image of the (Nb,V)C carbides; (c) Selected area diffraction (SAD) pattern; (d) STEM-HAADF micrograph of the (Nb,V)C carbide; (e) the schematic depiction of atom positions and the coherent and incoherent interfaces of the precipitates; (f) the inverse fast fourier transform (IFFT) of the inside the precipitate, (g) IFFT of (Nb,V)C carbides indicating misfit dislocations at the incoherent interface; (h) Atom probe tomography (APT) map reconstruction with grey, purple and blue which indicate C, V, and Nb atoms. (i) STEM-HAADF images of the (Nb,V)C carbides showing the atomic structure of the mixed-metal carbide. (For interpretation of the references to colour in this figure legend, the reader is referred to the web version of this article.)

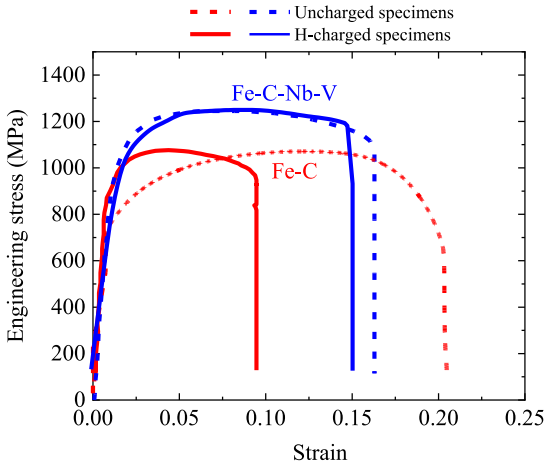

Fig. 4. Changes in engineering stress–strain curve with and without electrochemical hydrogen charging at the strain rate of $3.4 \times 10^{-6}\ s^{-1}$.

V sample is much smaller than the elongation loss for the Fe-C sample. This means that the mixed-metal precipitates play a beneficial role in mitigating the hydrogen embrittlement sensitivity. Fig. 4 also shows that with the addition of (Nb,V)C mixed-metal precipitates, the ultimate tensile strength and yield strength increase, while the elongation decreases only slightly, and by a reasonable amount (0.15 for H-charged Fe-C-Nb-V specimens).

The fracture surfaces of the H-charged and uncharged specimens are shown in Fig. 5. The fracture surface of the tensile tested H-charged Fe-C alloy contains intergranular cracks with a relatively smooth surface in the corner of the specimen. In a higher depth of the sample from the surface, the quasi-cleavage transgranular fracture surfaces with serrated markings were observed. It was already reported [54] that the low or high local hydrogen contents at potential flaws in martensitic steel can lead to quasi-cleavage and intergranular fracture features. In the current study, it is clear that the fracture mode is composed of transgranular quasi-cleavage fracture and intergranular fracture mode. In the corner of the fracture surface, a high amount of local hydrogen is present, leading to intergranular fracture, while in the higher depth of the sample, a lower content of absorbed hydrogen during SSRT leads to a lower local hydrogen content and quasi-cleavage fracture in the Fe-C steel. The intergranular cracking is a stress-controlled H-enhanced decohesion (HEDE) in the Fe-C alloy. This mechanism explains the reduction in cohesive bond strength between the atoms of the alloy in the presence of hydrogen and stress. The decohesion may occur when the critical hydrogen content is reached, and subsequently the crack initiation stage can be commenced in the preferred sites of decohesion, such as grain boundaries with high local hydrogen concentration. The HEDE mechanism can also assist the crack propagation. The relatively smooth facets in Fig. 5a show the intergranular crack, indicating the activation of the HEDE mechanism [10,55,56]. The serrated markings typical of quasi-cleavage fracture have also been found in other similar materials [52,57].

The fracture surface of the tensile-tested H-charged Fe-C-Nb-V specimen (Fig. 5c) contains no significant quasi-cleavage fracture

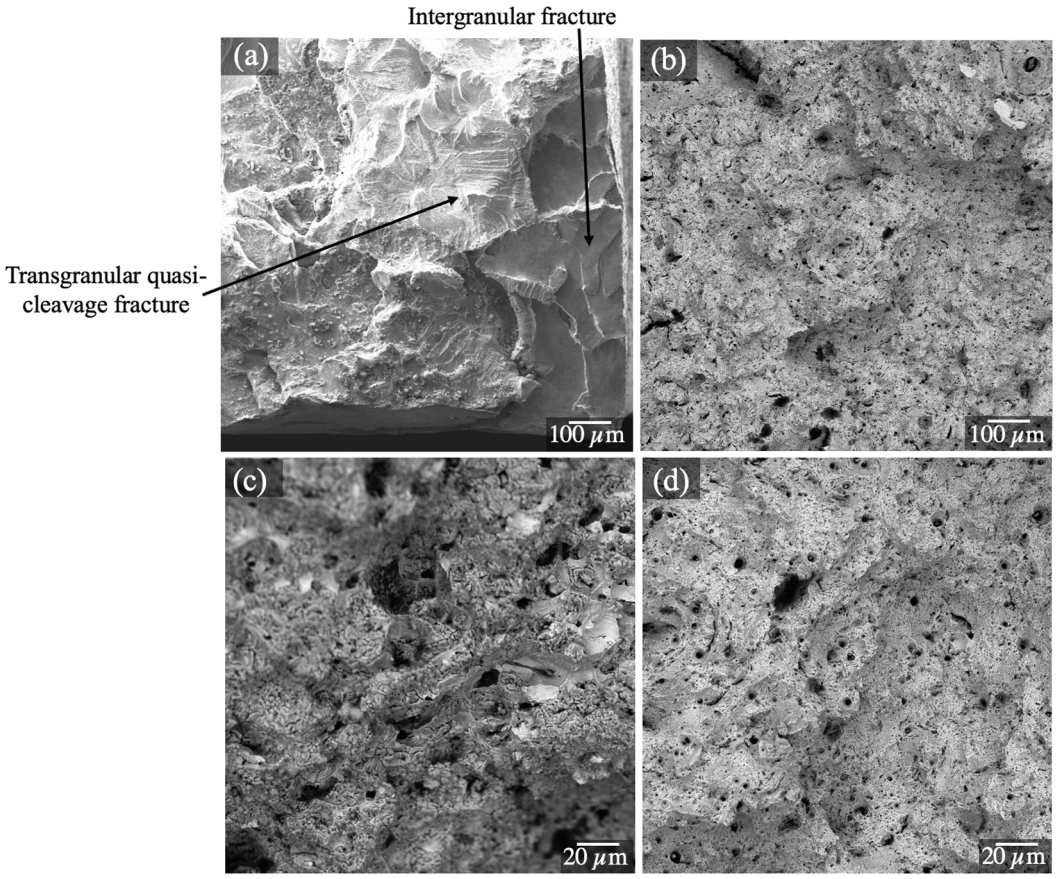

Fig. 5. The fracture surfaces of the tensile-tested H-charged and uncharged Fe-C and Fe-C-Nb-V specimens; (a) H-charged Fe-C specimen; (b) uncharged Fe-C specimen; (c) H-charged Fe-C-Nb-V specimen; and (d) uncharged Fe-C-Nb-V specimen.

features or intergranular crack indications, which is in good agreement with the SSRT results and demonstrates mitigated hydrogen embrittlement sensitivity. The fracture surfaces of the uncharged tensile tested Fe-C and Fe-C-Nb-V specimens (Fig. 5b,d) consist of dimples, indicating a dominance of ductile fracture features.

3.4. The nature of hydrogen trapping and distribution

Fig. 6 shows the TDS results of the H-charged specimens, at a constant heating rate. It is evident that different amounts of H are trapped in

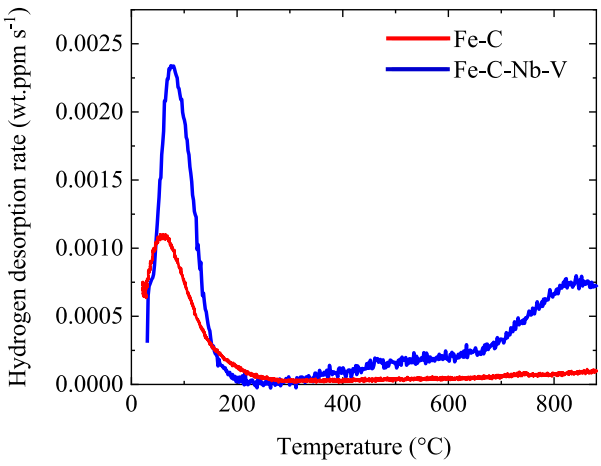

Fig. 6. TD spectra of the alloys and the corresponding peak deconvolution at heating rate of 300 K/h.

the two alloys at the same hydrogen charge time. Interestingly, there is a high-temperature peak in the Fe-C-Nb-V alloy that is absent in the thermal desorption (TD) of the Fe-C alloy. It is known that the distance of lattice diffusion of hydrogen from the different depths of the alloy at higher temperatures can form a misleading TDS peak resulting from the different distribution of hydrogen in the depth of the sample. We reduced the thickness of the sample to 0.5 mm to minimize the effect of thickness. To further clarify this effect, HES-XRD was used to qualitatively evaluate the distribution of hydrogen in the thickness of the sample. Diffusion of hydrogen leads to swelling of the crystal structure and introduction of additional residual stress. This residual stress due to hydrogen in the crystal structure is a response to the expansion of the lattice parameter of the alloy. The schematic illustration of the setup of the HES-XRD experimental station at DESY is shown in Fig. 7a. Fig. 7b shows the results of the HES-XRD measurement and the relative changes of the lattice parameter (the difference between the lattice parameters of the H-charged and the uncharged sample). The relative changes of lattice parameters in both alloys show the relatively uniform distribution of residual stress and thus the uniform distribution of hydrogen in the depth of the specimens for TDS measurements, importantly Fe-C-Nb-V. This means that in the TDS specimen, there is a uniform distribution of hydrogen in the depth of specimen and the distance of diffusion is not affecting the TDS results. Therefore, it is confirmed that the high-temperature peak is related to the high-energy trap site, and not to the hydrogen distribution profile in the alloy.

It has been found that partially obscured or overlapping thermal desorption (TD) peaks can vary the perceived height and width of the peaks [58]. Thus, there is the possibility of masking some peaks with other peaks, and it is necessary to analyze the TD spectra by fitting Gaussian functions, as shown in Fig. 8a and b. The results show that

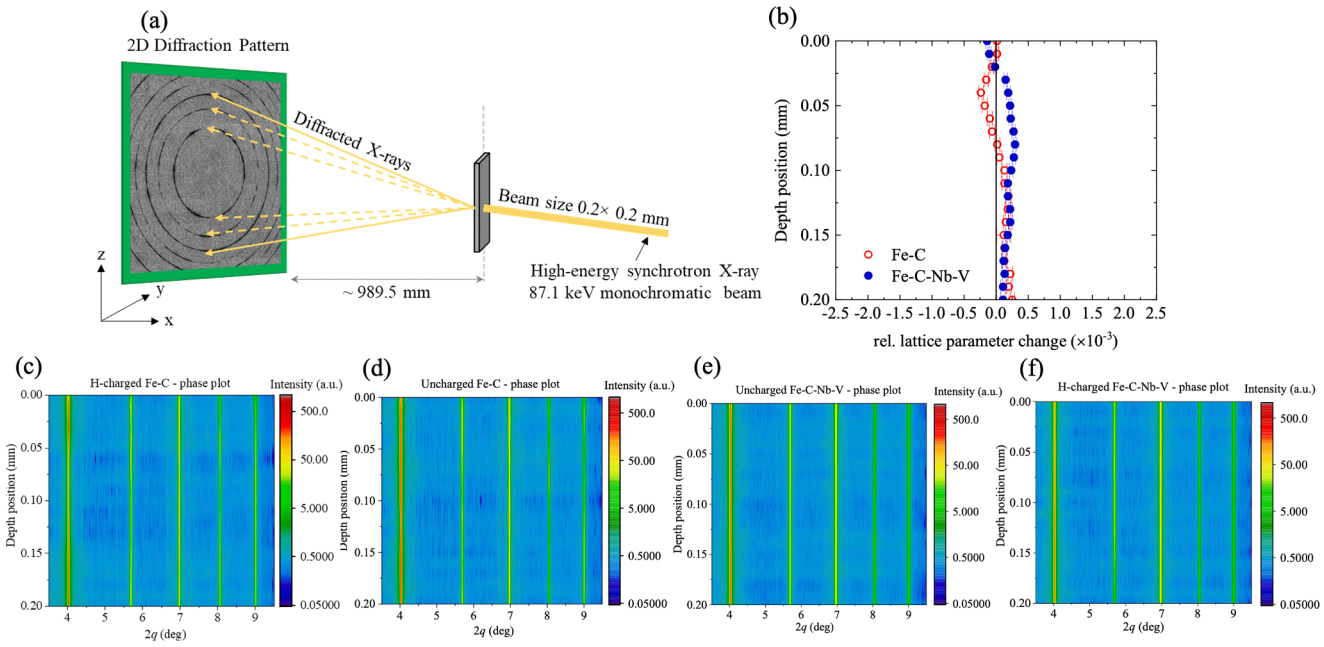

Fig. 7. (a) Schematic diagram showing the setup of high-energy synchrotron X-ray diffraction measurements at Deutsches Elektronen-Synchrotron (DESY) for a qualitative assessment of the H depth distribution due to H charging, (b) lattice constant measurements in the H-charged and uncharged specimens in the depth of the specimens by high-energy synchrotron X-ray beam for Fe-C and Fe-C-Nb-V specimens. The relative a_0 changes indicate the distribution profile of hydrogen in the alloys, (c-f) the diffraction patterns and the phase maps of the H-charged and uncharged specimens.

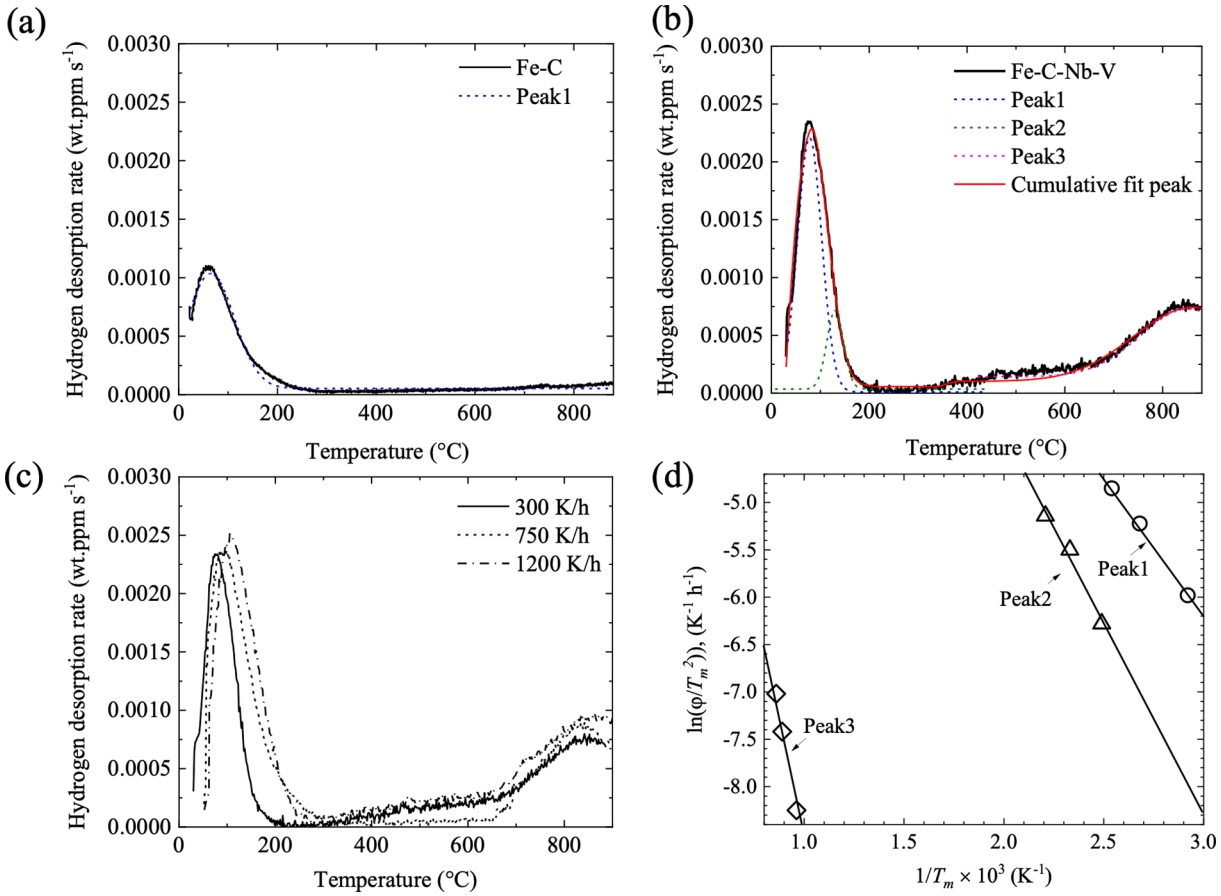

Fig. 8. Measured TD spectra and the peak deconvolution procedure for the heating rate of 300 K/h: (a) Fe-C and (b) Fe-C-Nb-V; (c) the desorption spectra in three different heating rates: 300, 750, and 1200 K/h, (d) thermally ramped desorption data calculated using Eq. (5) and Fig. (c), indicating the desorption energy of each trap as the slopes of the lines.

there is one peak in the TD spectra of the Fe-C alloy and three peaks in the TD spectra of the Fe-C-Nb-V alloy. The peaks corresponding to the Fe-C-Nb-V alloy are labeled as peak1, peak2 and peak3 in ascending temperature order. Fig. 8c shows the TD spectra at three different heating rates. Increasing the heating rate leads to shifting the peaks to higher temperatures. Based on Eq. (5) and the centers of the peaks in Fig. 8c, we could plot $\ln\left(\frac{\varphi}{T_m^2}\right)$ versus $\frac{1}{T_m}$, as shown in Fig. 8d. The slope of the line for each peak can be correlated with the desorption energy of each peak corresponding to a hydrogen trap. The obtained desorption energies are listed in Table 3.

Fig. 9 and Table 4 shows the permeation obtained electrochemical permeation results of the alloys. The higher trap density (N_T) in Fe-C-Nb-V alloy than that in the Fe-C alloy is in good agreement with the lower hydrogen diffusion coefficient in the Fe-C-Nb-V alloy. This means that higher trap density results in lower hydrogen diffusivity, which is consistent with the TDS results showing higher hydrogen trapping in the Fe-C-Nb-V alloy.

$D_{eff,1}$ *and* $D_{eff,2}$ for Fe–C-Nb–V alloy are smaller than those for the Fe-C alloy. The steady-state current densities and hydrogen fluxes observed in the first and second charging cycle are higher than for the Fe-C alloy. The comparatively high steady-state current and hydrogen flux resulted in a large Φ. The higher trap density (N_T) than in the Fe-C alloy is in good agreement with the lower hydrogen diffusion coefficient in the Fe-C-Nb-V alloy. This means that higher trap density results in lower hydrogen diffusivity, which is consistent with the TDS results showing higher hydrogen trapping in the Fe-C-Nb-V alloy.

4. Discussion

4.1. Hydrogen trapping state

While the TD spectra of the Fe-C alloy show only one hydrogen desorption peak, which can be associated with the hydrogen trapped in the basic martensitic structure [20,52], the TD spectra of the Fe-C-Nb-V alloys shows three hydrogen desorption peaks. The martensitic basic martensitic microstructure includes dislocations, grain boundaries, and the crystal lattice itself. Deconvolution of desorption spectra was not performed since in lath martensite microstructure there are several reversible hydrogen traps with low activation energies that consequently makes it complex to distinguish between them with very close desorption energies. It is rather postulated in literature that activation energy at low temperature is average value of desorption from these sites together, including also interstitial hydrogen in lattice [70]. The (Nb,V)C mixed-metal precipitates are semicoherent nano-size precipitates (STEM results in Fig. 3) with a relatively homogeneous distribution in the tempered martensitic structure. The coherency of the particles depends on their size and shape, which is correlated with the tempering temperature [20,21,24]. As can be seen in the TEM micrographs in Fig. 3, the (Nb,V)C mixed-metal precipitates are nano-sized disk-shaped with an average size of 12 nm. The results from APT show that the (Nb,V)C mixed-metal precipitates are disk-shaped with broad faces and thin sides. The IFFT results in Fig. 3 show that there are some misfit dislocations in side interface of the (Nb,V)C mixed-metal precipitates, while the smooth surface (broad interface) along (1 0 0) is coherent. This means that the (Nb,V)C mixed-metal precipitates are semicoherent, with an incoherent side interface and a coherent broad interface.

It has been previously reported that the broad faces of the disk-shape nanocarbides can act as hydrogen trap sites [13,39] which were found to be strong traps. Takahashi et al. [59] reported the observation of trapping of deuterium in APT, where some hydrogen had accumulated near the broad face of the disk-shaped nanocarbides. However, they did not investigate the precise origin of the trapped hydrogen. In another recent work [32], we have shown by DFT calculations that there is a relationship between the size of the interstitial sites at the coherent interface and the reversibility of the trapping sites. We found a very smooth coherent interface and very low coherency strain ($\frac{a_{dis}-a_{mat}}{a_{mat}}$) where a_{dis} and a_{mat} are the interplanar distances between the planes of the nanoparticles and matrix, respectively [21,32]. Therefore, the size of the interstitial sites at the coherent interface is similar to the matrix and they cannot be a strong trap site (similar to the interstitial lattice sites). Additionally, these interstitial sites (octahedral sites) at the interfaces were filled with carbon as indicated in APT results (Fig. 3h). Therefore, the broad coherent interface cannot be a strong trap site.

As can be seen in Fig. 3h in the results from APT, there is a carbon deficit in the mixed-metal precipitates, showing that there is a concentration of vacancies in the (Nb,V)C mixed-metal precipitates. In Fig. 3, we were able to show for the first time, direct evidence for these carbon vacancies by STEM-HAADF. In addition, it has already been reported that vacancies can be considered as high-energy hydrogen traps [17,20,31,60]. In the NaCl-type single-metal carbides, it has been reported that the carbon vacancies can be considered as strong irreversible hydrogen traps [17,48]. They also reported that in single-metal carbides, the irreversible hydrogen trap with a comparable desorption energy is related to carbon vacancies at the octahedral sites. Fig. 10 shows Kelvin probe force microscopy (SKPFM) after 8 and 120 h measuring times for the same area for each sample. After 8 h, the matrix has a lower potential than the particles. The observation of a bright area at the nanoparticles in the SKPFM images indicates that the nanocarbide traps more hydrogen than the matrix. After 120 h, the potential of the matrix and the particles on the side face of the nanocarbides decreased dramatically, while the potential of the broad face of the nanocarbides in this sample remained high. The presence of dark contrast in the potential maps after 120 h indicates a release of hydrogen from the matrix. The release of hydrogen from the broad face of the nanocarbides was not observed to any significant extent even after 120 h. While the broad face of the interface has a coherent smooth interface with a very low coherency strain, the very low hydrogen release from the broad face of the nanocarbides indicates that the hydrogen atoms are irreversibly trapped inside the particle since the face is broad and there is easy access without obstacle to the hydrogen trap sites inside the nanocarbides especially due to coherent borad interface. On the side face of the nanocarbides, it was observed that some misfit dislocations are present and can trap hydrogen, and avoid hydrogen to reach the precipitate.

When a part of coherency has been lost on the incoherent side, the elastic strain by lattice misfit has been reduced via the misfit dislocations (Fig. 3g), resulting in a weak elastic interaction of strain of misfit with the H atoms. This weak interaction leads to a consideable increase in H accumulation at misfit dislocations during SSRT in a hydrogen-containing environment. This indicates that the misfit dislocations (Fig. 3g) prevent hydrogen from entering the nanocarbide from the side interface. Therefore, in the SKPFM map cannot irreversibly trap the hydrogen, and the misfit dislocations and the side interface can act as a modest peak with intermediate energy for trapping the hydrogen. From the reported energies for this trapping site [17,59] and the calculated

Table 3
Summary of trapping data determined from thermal desorption spectroscopy (TDS).

peak	Approx. peak position [°C]	Trap site	Desorption energy, E_d [kJ/mol]
1	97	Basic martensitic microstructure*	28.1
2	176	Incoherent interface of (Nb,V)C mix-metal precipitates	43.2
3	761	Carbon vacancies at octahedral sites inside the (Nb,V)C mix-metal precipitates	87.3

*The basic martensitic microstructure included linear defects, lattice and grain boundaries.

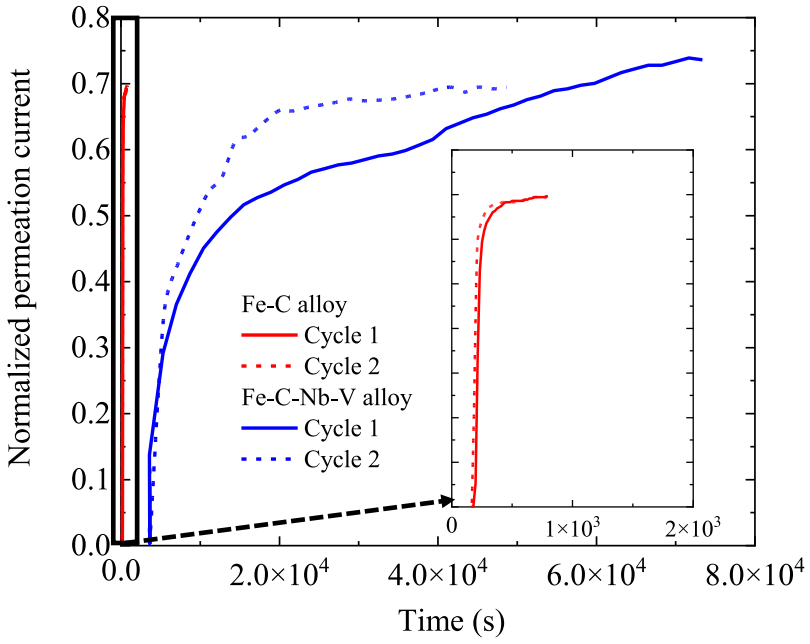

Fig. 9. Normalized permeation transients of Fe-C and Fe-C-V-Nb alloys.

Table 4
Electrochemical permeation results.

Material	$D_{eff,1}$	$I_{\infty,1}$	$i_{\infty,1}$	$j_{\infty,1}$	$D_{eff,2}$	$I_{\infty,2}$	$i_{\infty,2}$	$j_{\infty,2}$	Φ	N_T
	[cm^{-2} s^{-1}]	[μA]	[μA cm^{-2}]	[mol cm^{-2} s^{-1}]	[cm^{-2} s^{-1}]	[μA]	[μAcm^{-2}]	[mol cm^{-2} s^{-1}]	[mol cm^{-1} s^{-1}]	[cm^{-3}]
Fe-C	$2.18{\cdot}10^{-5}$	6.46	6.11	$6.36{\cdot}10^{-11}$	$2.72{\cdot}10^{-5}$	6.31	5.48	$5.72{\cdot}10^{-11}$	$6.18{\cdot}10^{-12}$	$1.22{\cdot}10^{18}$
Fe-C-Nb-V	$4.24{\cdot}10^{-7}$	33.38	31.43	$3.35{\cdot}10^{-10}$	$7.74{\cdot}10^{-7}$	15.43	13.81	$1.34{\cdot}10^{-10}$	$3.48{\cdot}10^{-11}$	$1.78{\cdot}10^{22}$

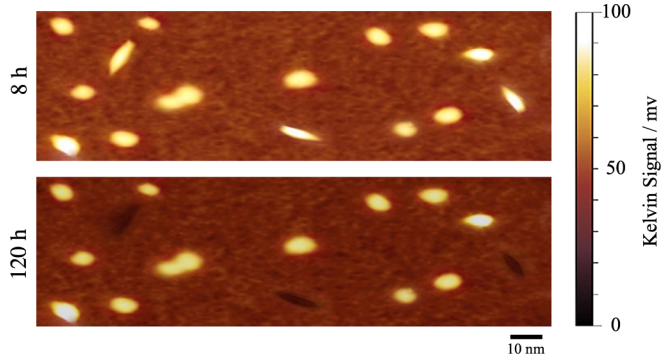

Fig. 10. SKPFM observations of the Fe-C-Nb-V alloy over the time; (a) 8 h; (b) 120 h.

desorption energy for peak2 compared to the references, it can be concluded that peak2 may originate from hydrogen trapped at the incoherent interface at the side face of the (Nb,V)C mixed-metal precipitates. The peak corresponding to H trapped at the side incoherent interface is the modest peak, indicating that the capacity to trap hydrogen at this site is small.

The results of DFT (Fig. 11) show that the octahedral sites (carbon vacancies) in the (Nb,V)C mixed-metal precipitates have negative solution energy for H, indicating that the trapping of hydrogen at the carbon vacancies at octahedral sites of the mixed-metal precipitates is favorable. The results from APT in Fig. 3f show that a higher carbon content has accumulated at the interface. Therefore, the octahedral sites of the interface are filled with carbon. The carbon vacancies inside the (Nb,V)C mixed-metal precipitates can be considered preferential hydrogen traps. Therefore, it is assumed that there are three hydrogen traps, namely the basic martensitic microstructure (peak1), the incoherent interface of the (Nb,V)C mixed-metal precipitates (peak2), and the carbon vacancies at octahedral sites inside the (Nb,V)C mixed-metal precipitates (peak3). In the next sections, we will discuss the mechanisms of HE susceptibility and its mitigation with the obtained results for the irreversibility of the hydrogen traps via the multiscale analysis approach.

4.2. *Hydrogen-assisted crack initiation and propagation behaviors*

Fig. 12 shows the SEM image of the microprinted specimen after H charging during tensile test and EBSD results of the area around a hydrogen-assisted secondary crack on the surface of the fractured charged tensile-tested Fe-C specimen parallel to the loading axis. We could not find any secondary crack in the H-charged tensile tested Fe-C-Nb-V alloy, which might be related to mitigation of hydrogen embrittlement in the alloy. It has already been reported that secondary crack cannot be observed in an alloy with mitigated hydrogen embrittlement [61,62]. Fig. 12a shows the analysis of hydrogen accumulation around the hydrogen-induced crack in Fe-C alloy using hydrogen microprint technique (HMPT) after tensile test in hydrogen environment. Fig. 12b,c shows the crack path in the IPF map and the boundary map after ion beam cleaning of the surface from the Ag particles. The results show that the crack path is not related to the orientation of the grains and the block or packet boundaries. There is also no evidence of retained austenite and carbide in the crack path as shown in Fig. 12d. The results from HES-XRD in Fig. 7 also confirm the presence of retained austenite in both alloys. The IPF map of parent austenite grains reconstructed using the Kurdjumov-Sachs orientation relationship model (Fig. 12f) shows that the hydrogen-assisted crack is passing along the PAGBs as an

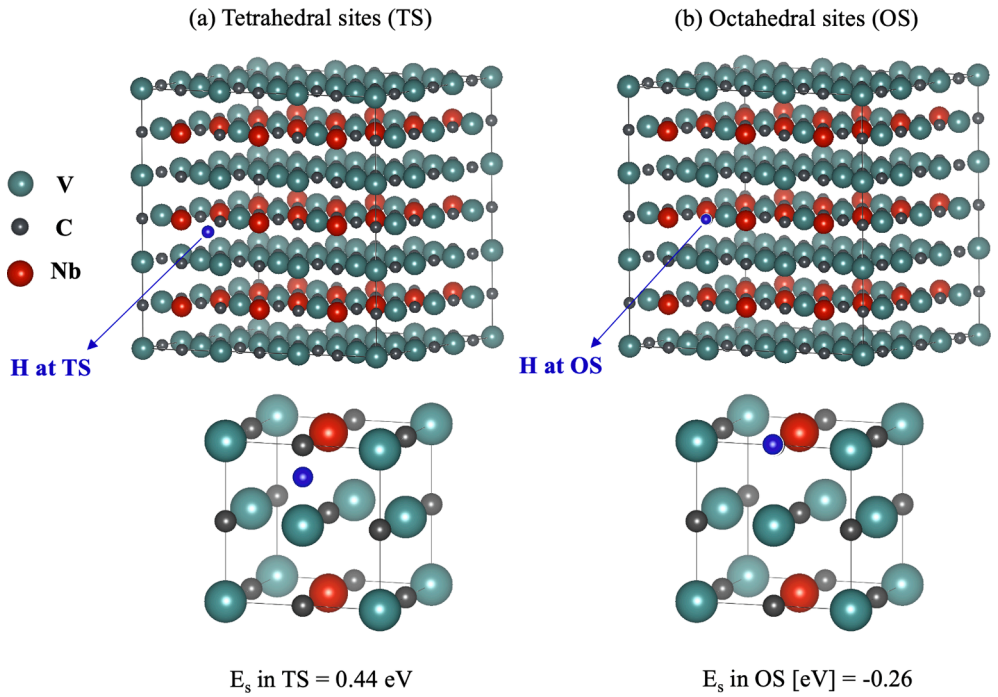

Fig. 11. (a) The tetrahedral site (TS) and (b) the octrahedral site (OS) that arises due to a C-vacancy in (Nb, V)C mix-metal carbides, including the enlarged figures showing the positions of the atoms and the solution energy calculated for the each one.

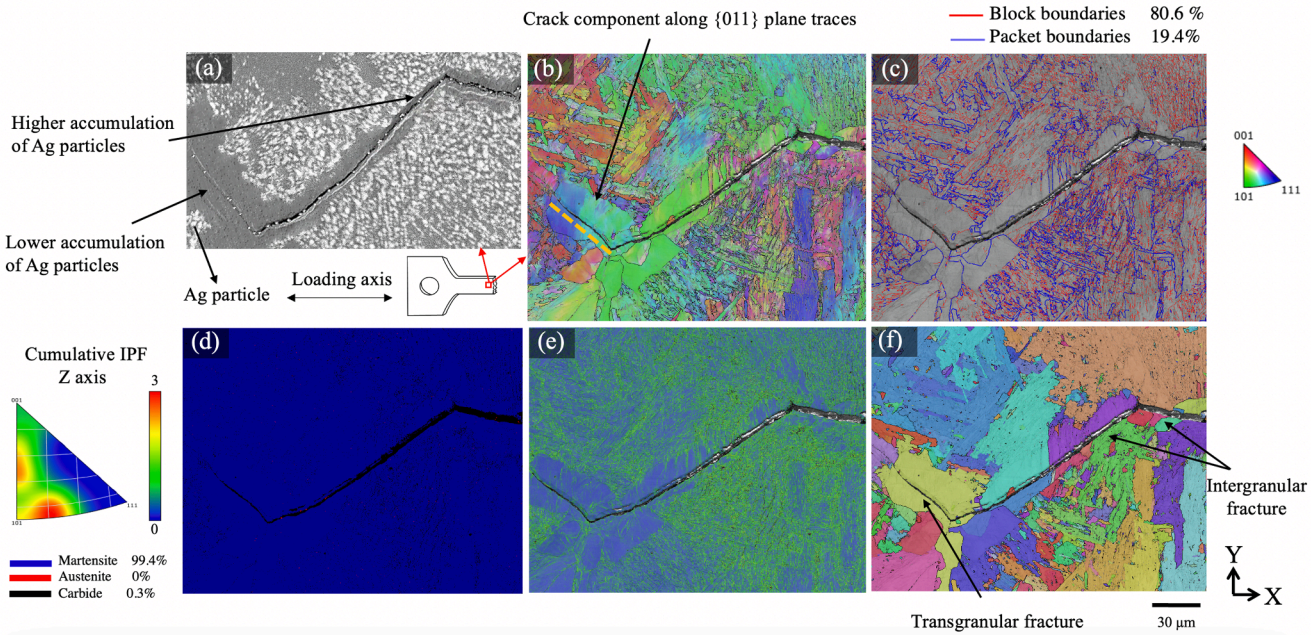

Fig. 12. (a) SEM image of the tensile tested specimen followed by HMPT around the H-assited crack path, (b-f) EBSD results of the tensile tested Fe-C specimen after ion beam cleaning of the surface from the Ag particles, showing the H-assisted crack path; (b) inverse pole figure (IPF) map of the child martensite microstructure; (c) the boundary map comprised of block and packet boundaries; (d) phase map; (e) Kernel average misorientation (KAM) map; and (f) the IPF map of the prior austenite grain (PAG) structure simulated by Kurdjumov-Sachs orientation relationship model.

intergranular crack and transgranular crack (the quasi-cleavage pattern). As discussed in section 3.3, the relatively smooth facets indicate the intergranular crack, suggesting the activation of the HEDE mechanism. In addition, the Kernel average misorientation (KAM) map in Fig. 12e shows the local misorientation gradient caused by the dislocations. In Fig. 12d, it can be seen that there is a high amount of dislocation accumulation around the crack path in some areas of the crack with intergranular character. The higher KAM value in the martensite substructure shows the high local strain and density of dislocations. The accumulation of dislocations close to the PAGBs forming the intergranular crack path is important evidence of the hydrogen embrittlement behavior of the Fe-C martensitic steel [63]. The grain boundaries are the preferential sites of accumulation of dislocation, and they are related to intergranular crack at PAGBs. We recently also reported [63] high accumulation of dislocations near the PAGBs and resulted high strain localization at the PAGBs. The weakly trapped

hydrogen in the dislocations close the PAGBs will play a role as a H source for the H-assisted intergranular crack. The combined HMPT result, KAM map, and IPF map of the PAGs in Fig. 12a, e, and f indicate a high hydrogen will be trapped at the dislocations near the PAGBs when the crack passes the PAGBs intergranularly. The weak trapping of hydrogen at the basic martensite microstructure, which also includes hydrogen trapped at dislocations, was studied and discussed in section 4.1. The reversibly trapped hydrogen at dislocations has been considered as a source of hydrogen for hydrogen assisted cracks [55,64,65]. By load increment during SSRT, the incremental opening of the PAGBs occurs. The local hydrogen concentration at the PAGBs increases continuously due to the supply of hydrogen via diffusion and/or the weakly trapped hydrogen near the PAGBs. In Fig. 12e,f, it can be seen that the intergranular cracking occurs at the PAGBs when the dislocations have accumulated near the crack that showing the H trapping at dislocations (Fig. 12a). However, when the crack is transgranular, the crack proceeds within the PAGs, which coincides with the low hydrogen trapping at dislocations and other weak H traps within the grain, implying that the weakly trapped hydrogen as a source of hydrogen cannot be only considered for the mechanism of the observed transgranular mechanism. This indicates that transgranular crack propagation does not only depend on the weakly trapped hydrogen, but also on the crystallographic features. The crystallographic features of the fracture plane of the hydrogen-induced transgranular crack are discussed in detail.

We performed a slip trace analysis based on the orientation data (Fig. 12b). The crack component that is transgranular crack is parallel to {0 1 1} plane traces (the orange dashed line in Fig. 12a). Our previous findings [52,57,63] also suggested that the {0 1 1} planes, which are slip planes in martensitic steel, can be associated with crack propagation along the {0 1 1} plane and thus can be arisen from hydrogen-enhanced slip localization. Although the analysis in Fig. 12 was a one-surface analysis and the exact orientation of the crack plane could not be determined, it is based on several previous studies, including our studies [44–47], one can conclude that the area consisting of {0 1 1} planes is related to quasi-cleavage fracture features. Fig. 13 shows the quasi-cleavage fracture surface including serrated markings in the tensile-tested Fe-C martensitic steel tensile tested under hydrogen environment, and the STEM micrograph of the lift-out lamella of the region indicated by a red line in Fig. 13(a), as well as the plane normal of the block boundary facets. Fig. 13(b) shows the facets that were separated by block boundaries. The block consists of many single-crystal laths. The normal direction of the facets between the block boundaries is calculated by obtaining the Kikuchi diffraction pattern. It can be seen that the facets run along the {0 1 1} planes, which is in good agreement with the orientation of the plane trace orientation in Fig. 12b. Nagao et al [66] show that the dominance of the {0 1 1} planes and the quasi-cleavage fracture pattern with serrated markings are related to dislocation activation and enhanced dislocation slip in the slip plane, which is related to hydrogen enhanced localized plasticity. The crystallographic features of the fracture plane of the hydrogen-induced transgranular crack indicate that the facets separated by block boundaries along the {0 1 1} planes are related to the quasi-cleavage fracture pattern with serrated markings. This indicates the activation of dislocations and enhanced dislocation slip in the {0 1 1} slip plane due to hydrogen-enhanced localized plasticity. The quasi-cleavage fracture occurred along the {0 1 1} planes in the current study and other other bcc and bct steels [52,57,63] indicates that fracture at the {0 1 1} plane is an intrinsic feature of hydrogen-induced quasi-cleavage fracture in bcc/bct steels

4.3. The mechanism of HE mitigation with addition of nanosized mixed-metal precipitates

The SSRT results (Fig. 4) show that the loss of ductility in the Fe-C-Nb-V alloy is significantly reduced, implying that the HE susceptibility is mitigated by the addition of (Nb,V)C mixed-metal precipitates. The TDS and electrochemical permeation results confirm that the trap density in the Fe-C-Nb-V alloy is higher than that in the Fe-C alloy. This high H trapping capacity can be related to the high trapping capacity resulting from the addition of (Nb,V)C mixed-metal precipitates. In Fig. 8, it can be seen that two additional peaks appear in the Fe-C-Nb-V alloy. Peak2 and peak3 exhibit higher hydrogen desorption energies resulting from the incoherent interface of the (Nb,V)C mixed-metal precipitates and the carbon vacancies at octahedral sites within the (Nb,V)C mixed-metal precipitates (43.2 and 87.3 kJ.mol^{-1}, respectively). These energies indicate that the higher density of H-traps in the Fe-C-Nb-V alloy is accompanied by the introduction of higher energy H-traps. This leads to a higher proportion of irreversible hydrogen atoms in the Fe-C-Nb-V alloy compared to the Fe-C alloy with hydrogen inclusions in the basic martensitic structure. It is known that a high fraction of irreversible hydrogen atoms in an alloy reduces the possibility of reaching diffusible hydrogen to a potential flaw and/or crack tip to allow crack initiation and/or propagation. Between these trapped hydrogen atoms at peak2 and peak3 (trapped hydrogen at the trap sites introduced by the mixed-metal precipitates), carbon vacancies at octahedral sites within the (Nb,V)C mixed-metal precipitates are associated with peak3, representing the relatively irreversible hydrogen content in the Fe-C-Nb-V alloy.

While the fracture surface of the tensile-tested Fe-C alloy with hydrogen charging shows the intergranular cracks and quasi-cleavage fracture features, the fracture surface of the F-C-Nb-V alloy consists of dimples indicating a ductile fracture feature. These results of the crack

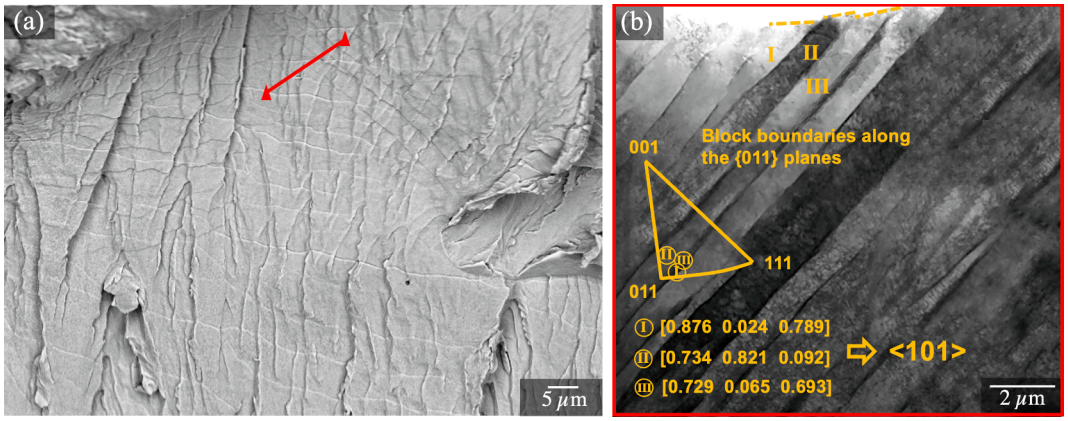

Fig. 13. (a) The quasi cleavage fracture surface of the H-charged Fe-C alloy, (b) STEM micrograph of the lift-out lamella of the area indicated in Fig. 13(a) by red line, and the plane normal of the block boundary facets. (For interpretation of the references to colour in this figure legend, the reader is referred to the web version of this article.)

path studies in Fig. 12 indicate that the available weakly trapped hydrogen near the PAGBs in the Fe-C alloy is mainly trapped at the dislocations around PAGBs, suggesting a hydrogen-enhanced decohesion mechanism. This low-energy trapped hydrogen at the dislocations around the PAGBs is the H source for the H-assisted crack. This accumulated H source can provide more hydrogen to the potential flaw (such as the PAGBs). Several studies have reported that a global concept for hydrogen embrittlement is the necessity of building up a critical local H concentration at flaw before crack initiation [10,12]. Hydrogen accumulation at the flaws i.e., the PAGBs, during in situ hydrogen charging would increase, leading to weakening of cohesive interatomic bonds and eventual separation of atoms during tensile loading and the eventual initiation of PAGB cracks [64,66–68]. The microcracks may also form due to hydrogen-enhanced localized plasticity when the local hydrogen content is lower and quasi-cleavage fracture features with serrated markings form along certain {0 1 1} crystallographic planes (Fig. 5a, 12, and 13).

Fig. 14 summarizes the mechanism of mitigation of hydrogen embrittlement in the Fe-Nb-V-C alloy. According to the obtained results, the promising hydrogen embrittlement behavior of the Fe-C-Nb-V alloy is due to the following reasons, which are determined by the nature of the trap sites and the microstructural features: (i) a higher fraction of irreversible hydrogen traps indicates that the strong hydrogen trapping sites in this alloy prevent the hydrogen at the potential flaws from reaching the critical concentration required for crack nucleation [9,12,69] and a lower possibility of dislocation activation and enhanced dislocation slip in the {0 1 1} slip plane due to the localized plasticity enhanced by hydrogen at lower local hydrogen content. (ii) As seen in the EBSD results, the addition of the (Nb,V)C mixed metal refines the PAGs in the Fe-C-Nb-V alloy by pinning the grain boundaries. The high total length of the PAGBs in the Fe-C-Nb-V alloy and the high fraction of irreversible hydrogen traps in the alloy leads to a decrease in the normalized H content in the PAGB unit length in the Fe-C-Nb-V alloy. A widely accepted mechanism for hydrogen embrittlement is that some critical hydrogen content accumulates at potential flaws to initiate cracking. The nature of trap sites and high total length of the PAGBs in the Fe-C-Nb-V alloy mean that the possibility of building up critical local hydrogen content at the PAGBs for intergranular hydrogen-assisted cracking is reduced due to the hydrogen-enhanced decohesion mechanism, thus improving the hydrogen embrittlement behavior of the alloy.

In addition, less weakly trapped hydrogen in the alloy increases the possibility of dislocation activation and enhanced dislocation slip in the {0 1 1} slip plane due to hydrogen-enhanced localized plasticity in the areas with affinity for transgranular hydrogen-assisted cracking at lower local hydrogen content.

5. Conclusions

The following conclusions can be deducted from this study:

1- The (Nb,V)C mixed metal nanocarbides act as irreversible hydrogen traps by trapping hydrogen at carbon vacancies in the nanoscale mixed-metal precipitates, which can effectively trap hydrogen and prevent hydrogen from reaching the potential flaws, e.g. PAGBs, to reduce the possibility for HE caused by high local hydrogen concentration. In lower local hydrogen contents, the high fraction of irreversible H traps can reduce the possibility of dislocation activation and enhanced dislocation slip in the {0 1 1} slip plane due to the localized plasticity enhanced by hydrogen.

2- The high total length of PAGBs in Fe-C-Nb-V alloy due to grain refinement by (Nb,V)C mixed-metal precipitates and the high fraction of irreversible hydrogen traps in the alloy leads to a decrease in the normalized H content in the unit length of the PAGBs, and thus to a lower probability of H-assisted cracking.

3- In the Fe-C alloy, hydrogen-assisted cracks start at the PAGBs and propagate along the {0 1 1} planes, forming a quasi-cleavage fracture pattern. A detailed crystallographic study was performed and the mechanism of H-assisted transgranular fracture was explained.

4- In the martensitic Fe-C steel, the coexistance of HEDE and HELP mechanims was observed depending on the local hydrogen content.

5- Direct evidence for the carbon vacancies in the novel nano-precipitates is observed for the first time via HAADF-STEM. The SKPFM results indicate that the broad face of the novel nano-precipitates has an irreversible hydrogen trapping character. The smooth, coherent broad interface paves the way to access the high-energy trap sites in the carbon vacancies inside the novel mixed-metal precipitates. Calculations from DFT have shown that trapping at the carbon vacancies at octahedral sites of the nano-precipitates is energetically favorable and preferable.

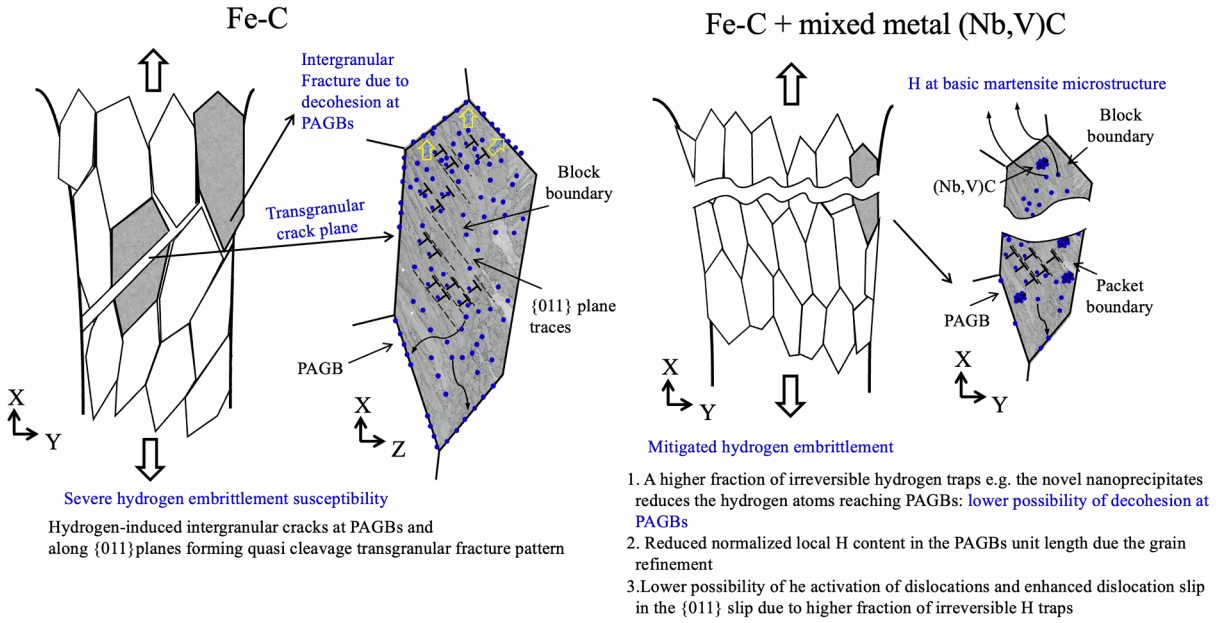

Fig. 14. Schematic illustrations of the hydrogen embrittlement behaviour of the Fe-C and Fe-C-Nb-V specimens.

Declaration of Competing Interest

The authors declare that they have no known competing financial interests or personal relationships that could have appeared to influence the work reported in this paper.

Data availability

Data will be made available on request.

Acknowledgement

The authors would like to acknowledge the financial contribution of Kamei Corporation, Japan, and the Ministry of Education, Culture, Sports, Science and Technology, Japan (MEXT- Monbu Kagakushu). The authors appreciate the helpful discussion and resources provided by F. Abbasi. We acknowledge DESY (Hamburg, Germany), a member of the Helmholtz Association HGF, for the provision of experimental facilities. Parts of this research were carried out at PETRA III and we would like to thank Dr. Norbert Schell for assistance in using beamline P07b.

Appendix 1

Density functional theory (DFT) calculation of the solution energies of the different ratios of Nb and V at octahedral (OS) and tetrahedral (TS) sites.

Carbide type	E_s in OS [eV]	E_s in TS [eV]
$Nb_{0.75}V_{0.25}C$	−0.32517	1.68281575
$Nb_{0.5}V_{0.5}C$	−0.2869	1.09579863
$Nb_{0.25}V_{0.75}C$	−0.26064	0.44234516

Solution energies have been calculated relative to H in ferrite (αFe).

$$\Delta E_{sol} = \left(NbVC_{wH} - NbVC_{w/oH}\right) - \left(\alpha Fe_{wH} - \alpha Fe_{w/oH}\right)$$

Where $NbVC_{wH}$ is the cell with H and $NbVC_{w/oH}$ without. There have been no stable TS for $Nb_{0.5}V_{0.5}C$ and $Nb_{0.25}V_{0.75}C$. H was pushed into the more stable trigonal sites.

References

[1] J. Zhao, Z. Jiang, C.S. Lee, Effects of tungsten on the hydrogen embrittlement behaviour of microalloyed steels, Corrosion Science 82 (2014) 380–391, https://doi.org/10.1016/j.corsci.2014.01.042.
[2] H.-J. Kim, S.-H. Jeon, W.-S. Yang, B.-G. Yoo, Y.-D. Chung, H.-Y. Ha, H.-Y. Chung, Effects of titanium content on hydrogen embrittlement susceptibility of hot-stamped boron steels, Journal of Alloys and Compounds 735 (2018) 2067–2080, https://doi.org/10.1016/j.jallcom.2017.12.004.
[3] S. Zhang, Y. Huang, B. Sun, Q. Liao, H. Lu, B. Jian, H. Mohrbacher, W. Zhang, A. Guo, Y. Zhang, Effect of nb on hydrogen-induced delayed fracture in high strength hot stamping steels, Materials Science and Engineering A 626 (2015) 136–143, https://doi.org/10.1016/j.msea.2014.12.051.
[4] J. Lee, T. Lee, D.-J. Mun, C.M. Bae, C.S. Lee, Comparative study on the effects of cr, v, and mo carbides for hydrogen-embrittlement resistance of tempered martensitic steel, Scientific Reports 9 (2019) 1–9.
[5] M. Gómez, S.F. Medina, Role of microalloying elements in the microstructure of hot rolled steels, International Journal of Materials Research 102 (2011) 1197–1207, https://doi.org/10.3139/146.110585.
[6] H. Najafi, J. Rassizadehghani, S. Asgari, As-cast mechanical properties of vanadium/niobium microalloyed steels, Materials Science and Engineering A 486 (2008) 1–7, https://doi.org/10.1016/j.msea.2007.08.057.
[7] S. Shanmugam, M. Tanniru, R.D.K. Misra, D. Panda, S. Jansto, Precipitation in v bearing microalloyed steel containing low concentrations of Ti and nb, Materials Science and Technology 21 (2005) 883–892, https://doi.org/10.1179/174328405X47564.
[8] X. Li, X. Ma, S.V. Subramanian, C. Shang, R.D.K. Misra, influence of prior austenite grain size on martensite–austenite constituent and toughness in the heat affected zone of 700MPa high strength linepipe steel, Materials Science and Engineering A 616 (2014) 141–147, https://doi.org/10.1016/j.msea.2014.07.100.
[9] M. Safyari, M. Moshtaghi, S. Kuramoto, On the role of traps in the microstructural control of environmental hydrogen embrittlement of a 7xxx series aluminum alloy, Journal of Alloys and Compounds 855 (2021), 157300, https://doi.org/10.1016/j.jallcom.2020.157300.
[10] M. Safyari, M. Moshtaghi, S. Kuramoto, Environmental hydrogen embrittlement associated with decohesion and void formation at soluble coarse particles in a cold-rolled al–Cu based alloy, Materials Science and Engineering A 799 (2021), 139850, https://doi.org/10.1016/j.msea.2020.139850.
[11] I. Maroef, D.L. Olson, M. Eberhart, G.R. Edwards, Hydrogen trapping in ferritic steel weld metal, International Materials Review 47 (2002) 191–223, https://doi.org/10.1179/095066002225006548.
[12] G.M. Pressouyre, Trap theory of hydrogen embrittlement, Acta Metallurgica 28 (1980) 895–911, https://doi.org/10.1016/0001-6160(80)90106-6.
[13] H. Asahi, D. Hirakami, S. Yamasaki, Hydrogen trapping behavior in vanadium-added steel, ISIJ International 43 (2003) 527–533, https://doi.org/10.2355/isijinternational.43.527.
[14] T. Asaoka, G. Lapasset, M. Aucouturier, P. Lacombe, Observation of hydrogen trapping in Fe-0.15 wt% Ti alloy by high resolution autoradiography, Corrosion 34 (1978) 39–47, https://doi.org/10.5006/0010-9312-34.2.39.
[15] H.G. Lee, J.-Y. Lee, Hydrogen trapping by TiC particles in iron, Acta Metallurgica 32 (1984) 131–136, https://doi.org/10.1016/0001-6160(84)90210-4.
[16] M. Ohnuma, J. Suzuki, F.-G. Wei, K. Tsuzaki, Direct observation of hydrogen trapped by NbC in steel using small-angle neutron scattering, Scripta Materialia 58 (2008) 142–145, https://doi.org/10.1016/j.scriptamat.2007.09.026.
[17] F.G. Wei, K. Tsuzaki, Quantitative analysis on hydrogen trapping of TiC particles in steel, Metallurgical and Materials Transactions A: Physical Metallurgy and Materials Science 37 (2006) 331–353, https://doi.org/10.1007/s11661-006-0004-3.
[18] J. Lee, T. Lee, Y.J. Kwon, D.-J. Mun, J.-Y. Yoo, C.S. Lee, Role of mo/V carbides in hydrogen embrittlement of tempered martensitic steel, Corrosion Reviews 33 (2015) 433–441, https://doi.org/10.1515/corrrev-2015-0052.
[19] F.G. Wei, T. Hara, K. Tsuzaki, Precise determination of the activation energy for desorption of hydrogen in two ti-added steels by a single thermal-desorption spectrum, Metallurgical and Materials Transactions B 35 (2004) 587–597, https://doi.org/10.1007/s11663-004-0057-x.
[20] F.G. Wei, K. Tsuzaki, gaseous HE of materials in energy technologies, gaseous hydrog, Embrittlement Mater. Energy Technol. 1 (2012) 493e525.
[21] W. Qin, J.A. Szpunar, A general model for hydrogen trapping at the inclusion-matrix interface and its relation to crack initiation, Philosophical Magazine 97 (2017) 3296–3316, https://doi.org/10.1080/14786435.2017.1378451.
[22] S. Zhang, J. Wan, Q. Zhao, J. Liu, F. Huang, Y. Huang, X. Li, Dual role of nanosized NbC precipitates in hydrogen embrittlement susceptibility of lath martensitic steel, Corrosion Science 164 (2020), 108345.
[23] J. Lee, T. Lee, Y.J. Kwon, D.-J. Mun, J.-Y. Yoo, C.S. Lee, Effects of vanadium carbides on hydrogen embrittlement of tempered martensitic steel, Metals and Materials International 22 (3) (2016) 364–372.
[24] M. Safyari, M. Moshtaghi, T. Hojo, E. Akiyama, Mechanisms of hydrogen embrittlement in high-strength aluminum alloys containing coherent or incoherent dispersoids, Corrosion Science 194 (2022) 109895.
[25] N. Hansen, Hall-Petch relation and boundary strengthening, Scripta Materialia 51 (8) (2004) 801–806.
[26] K.R. Limmer, First-principles investigations of iron-based alloys and their properties, Missouri University of Science and Technology, 2014.
[27] L. Adnane, R. Kesri, S. Hamar-Thibault, vanadium carbides formed from the melt by solidification in fe V x C alloys (X cr, mo, nb), Journal of Alloys and Compounds 178 (1992) 71–84, https://doi.org/10.1016/0925-8388(92)90248-8.
[28] R. Kesri, S. Hamar-Thibault, Structures ordonnees a longue distance dans les carbures mc dans les fontes, Acta Metallurgica 36 (1) (1988) 149–166.

[29] A. Turk, D. San Martín, P.E.J. Rivera-Díaz-del-Castillo, E.I. Galindo-Nava, Correlation between vanadium carbide size and hydrogen trapping in ferritic steel, Scripta Materialia 152 (2018) 112–116, https://doi.org/10.1016/j.scriptamat.2018.04.013.
[30] F.-G. Wei, T. Hara, K. Tsuzaki, Nano-preciptates design with hydrogen trapping character in high strength steel, Adv. Steels, Springer, in, 2011, pp. 87–92.
[31] M. Moshtaghi, B. Loder, M. Safyari, T. Willidal, T. Hojo, G. Mori, Hydrogen trapping and desorption affected by ferrite grain boundary types in shielded metal and flux-cored arc weldments with ni addition, Int. J. Hydrog. Energy. 47 (47) (2022) 20676–20683.
[32] M. Safyari, N. Khossossi, T. Meisel, P. Dey, T. Prohaska, M. Moshtaghi, New insights into hydrogen trapping and embrittlement in high strength aluminum alloys, Corrosion Science 223 (2023) 111453.
[33] L. Lan, X. Kong, Z. Hu, C. Qiu, D. Zhao, L. Du, Hydrogen permeation behavior in relation to microstructural evolution of low carbon bainitic steel weldments, Corrosion Science 112 (2016) 180–193, https://doi.org/10.1016/j.corsci.2016.07.025.
[34] M. Moshtaghi, M. Safyari, G. Mori, hydrogen absorption rate and hydrogen diffusion in a ferritic steel coated with a micro- or nanostructured ZnNi coating, Electrochemistry Communications 134 (2022), 107169, https://doi.org/10.1016/j.elecom.2021.107169.
[35] W.Y. Choo, J.Y. Lee, Thermal analysis of trapped hydrogen in pure iron, Metallurgical Transactions A 13 (1982) 135–140, https://doi.org/10.1007/BF02642424.
[36] M. Moshtaghi, M. Safyari, S. Kuramoto, T. Hojo, Unraveling the effect of dislocations and deformation-induced boundaries on environmental hydrogen embrittlement behavior of a cold-rolled al–Zn–Mg–Cu alloy, Int. J. Hydrog. Energy. 46 (2021) 8285–8299, https://doi.org/10.1016/j.ijhydene.2020.12.028.
[37] P. Gong, E.J. Palmiere, W.M. Rainforth, Dissolution and precipitation behaviour in steels microalloyed with niobium during thermomechanical processing, Acta Materialia 97 (2015) 392–403.
[38] T.J. Harrington, J. Gild, P. Sarker, C. Toher, C.M. Rost, O.F. Dippo, C. McElfresh, K. Kaufmann, E. Marin, L. Borowski, P.E. Hopkins, J. Luo, S. Curtarolo, D. W. Brenner, K.S. Vecchio, Phase stability and mechanical properties of novel high entropy transition metal carbides, Acta Materialia 166 (2019) 271–280.
[39] M. Moshtaghi, M. Safyari, Effect of Work-Hardening mechanisms in asymmetrically Cyclic-Loaded austenitic stainless steels on Low-Cycle and High-Cycle fatigue behavior, Steel Research International 92 (2021) 2000242, https://doi.org/10.1002/srin.202000242.
[40] P. Xu, C. Li, W. Li, M. Zhu, W. Li, K. Zhang, Effect of microstructure on hydrogen embrittlement susceptibility in quenching-partitioning-tempering steel, Materials Science and Engineering A 831 (2022), 142046, https://doi.org/10.1016/j.msea.2021.142046.
[41] X. Song, D. Huang, W. Jia, Y. Liu, J. Gao, Y. Ren, T. Ma, in-situ high-energy x-ray diffraction study of the early-stage decomposition in 2:17-type Sm-Co-based permanent magnets, Acta Materialia 244 (2023), 118580, https://doi.org/10.1016/j.actamat.2022.118580.
[42] S. Antonov, E. Sun, S. Tin, Synchrotron in-Situ aging study and correlations to the γ′ phase instabilities in a High-Refractory content γ-γ′ Ni-Base superalloy, Metallurgical and Materials Transactions A: Physical Metallurgy and Materials Science 49 (2018) 3885–3895, https://doi.org/10.1007/s11661-018-4683-3.
[43] M.J. Crooks, A.J. Garratt-Reed, J.B.V. Sande, W.S. Owen, Precipitation and recrystallization in some vanadium and vanadium-niobium microalloyed steels, Metallurgical Transactions A 12 (12) (1981) 1999–2013.
[44] Q.D. Liu, W.Q. Liu, S.J. Zhao, Solute behavior in the initial nucleation of v- and Nb-Containing carbide, Metallurgical and Materials Transactions A: Physical Metallurgy and Materials Science 42 (2011) 3952–3960, https://doi.org/10.1007/s11661-011-0783-z.
[45] C. Zhao, X. Xing, J. Guo, Z. Shi, Y. Zhou, X. Ren, Q. Yang, Micro-properties of (Nb, m)C carbide (M= v, mo, w and cr) and precipitation behavior of (Nb, v)C in carbide reinforced coating, Journal of Alloys and Compounds 788 (2019) 852–860, https://doi.org/10.1016/j.jallcom.2019.02.284.
[46] S.N. Kulkov, S.A. Vorozhtsov, Structure and mechanical behavior of Al–Al4C3 composites, Russian Physics Journal 53 (2011) 1153–1157, https://doi.org/10.1007/s11182-011-9544-0.
[47] M. Mizumoto, Y. Tajima, A. Kagawa, Thermal expansion behavior of SiCP/Aluminum alloy composites fabricated by a Low-Pressure infiltration process, Materials Transactions 45 (2004) 1769–1773, https://doi.org/10.2320/matertrans.45.1769.
[48] F.G. Wei, K. Tsuzaki, Hydrogen trapping phenomena in martensitic steels, in: Gaseous Hydrog. Embrittlement Mater. Energy Technol., Elsevier, 2012: pp. 493–525.
[49] J. Takahashi, K. Kawakami, Y. Kobayashi, Quantitative analysis of carbon content in cementite in steel by atom probe tomography, Ultramicroscopy 111 (2011) 1233–1238, https://doi.org/10.1016/j.ultramic.2011.03.024.
[50] M. Thuvander, J. Weidow, J. Angseryd, L.K.L. Falk, F. Liu, M. Sonestedt, K. Stiller, H.-O. Andrén, Quantitative atom probe analysis of carbides, Ultramicroscopy 111 (2011) 604–608, https://doi.org/10.1016/j.ultramic.2010.12.024.
[51] Y. Ou, Y. Jiang, Y. Wang, Z. Liu, A. Lervik, R. Holmestad, Vacancy and solute co-segregated η1 interface in over-aged Al-Zn-Mg alloys, Acta Materialia 218 (2021), 117082, https://doi.org/10.1016/j.actamat.2021.117082.
[52] M. Moshtaghi, M. Safyari, Temperature mitigates the hydrogen embrittlement sensitivity of martensitic steels in slow strain rates, Vacuum 202 (2022), 111187, https://doi.org/10.1016/j.vacuum.2022.111187.
[53] M.L. Martin, M. Dadfarnia, A. Nagao, S. Wang, P. Sofronis, Enumeration of the hydrogen-enhanced localized plasticity mechanism for hydrogen embrittlement in structural materials, Acta Materialia 165 (2019) 734–750.
[54] A. Shibata, T. Yonemura, Y. Momotani, M. Park, S. Takagi, Y. Madi, J. Besson, N. Tsuji, Effects of local stress, strain, and hydrogen content on hydrogen-related fracture behavior in low-carbon martensitic steel, Acta Materialia 210 (2021), 116828, https://doi.org/10.1016/j.actamat.2021.116828.
[55] A.R. Troiano, the role of hydrogen and other interstitials in the mechanical behavior of metals, Trans ASM. 52 (1960) 54–80.
[56] Y. Liang, P. Sofronis, Toward a phenomenological description of hydrogen-induced decohesion at particle/matrix interfaces, Journal of the Mechanics and Physics of Solids 51 (2003) 1509–1531, https://doi.org/10.1016/S0022-5096(03)00052-8.
[57] S. Pichler, A. Bendo, G. Mori, M. Safyari, M. Moshtaghi, Inhibition of grain growth by pearlite improves hydrogen embrittlement susceptibility of the ultra-low carbon ferritic steel: the influence of h-assisted crack initiation and propagation mechanisms, Journal of Materials Science 58 (2023) 13460–13475, https://doi.org/10.1007/s10853-023-08856-y.
[58] P. Novak, R. Yuan, B.P. Somerday, P. Sofronis, R.O. Ritchie, A statistical, physical-based, micro-mechanical model of hydrogen-induced intergranular fracture in steel, Journal of the Mechanics and Physics of Solids 58 (2010) 206–226, https://doi.org/10.1016/j.jmps.2009.10.005.
[59] J. Takahashi, K. Kawakami, Y. Kobayashi, T. Tarui, The first direct observation of hydrogen trapping sites in TiC precipitation-hardening steel through atom probe tomography, Scripta Materialia 63 (2010) 261–264, https://doi.org/10.1016/j.scriptamat.2010.03.012.
[60] M. Moshtaghi, M. Safyari, G. Mori, Combined thermal desorption spectroscopy, hydrogen visualization, HRTEM and EBSD investigation of a ni–Fe–Cr alloy: The role of hydrogen trapping behavior in hydrogen-assisted fracture, Materials Science and Engineering A 848 (2022), 143428, https://doi.org/10.1016/j.msea.2022.143428.
[61] A. Nagao, C.D. Smith, M. Dadfarnia, P. Sofronis, I.M. Robertson, The role of hydrogen in hydrogen embrittlement fracture of lath martensitic steel, Acta Materialia 60 (2012) 5182–5189, https://doi.org/10.1016/j.actamat.2012.06.040.
[62] L. Cho, P.E. Bradley, D.S. Lauria, M.J. Connolly, E.J. Seo, K.O. Findley, J.G. Speer, L. Golem, A.J. Slifka, Effects of hydrogen pressure and prior austenite grain size on the hydrogen embrittlement characteristics of a press-hardened martensitic steel, Int. J. Hydrog. Energy. 46 (47) (2021) 24425–24439.
[63] M. Moshtaghi, M. Safyari, Different augmentations of absorbed hydrogen under elastic straining in high-pressure gaseous hydrogen environment by as-quenched and as-tempered martensitic steels: combined experimental and simulation study, Int. J. Hydrog. Energy. 48 (70) (2023) 27408–27415.
[64] R.A. Oriani, The diffusion and trapping of hydrogen in steel, Acta Metallurgica 18 (1970) 147–157, https://doi.org/10.1016/0001-6160(70)90078-7.
[65] W.W. Gerberich, P.G. Marsh, J.W. Hoehn, Hydrogen Effects in Materials, TMS Warrendale PA. (1996) 539–551.
[66] I.M. Robertson, P. Sofronis, A. Nagao, M.L. Martin, S. Wang, D.W. Gross, K. E. Nygren, Hydrogen embrittlement understood, Metallurgical and Materials Transactions A: Physical Metallurgy and Materials Science 46 (6) (2015) 2323–2341.
[67] I.M. BERNSTEIN, A.W. THOMPSON, Hydrogen effects in metals, Warrendale PA Metall. Soc. AIME 1981 1071 P. (1981).
[68] C.J. McMahon, Hydrogen-induced intergranular fracture of steels, Engineering Fracture Mechanics 68 (6) (2001) 773–788.
[69] E. Akiyama, S. Matsuoka, Hydrogen visualization in steels using ag decoration method, Materials Transactions 56 (2015) 793–797, https://doi.org/10.2320/matertrans.M2014431.
[70] K. Takai, R. Watanuki, Hydrogen in Trapping States Innocuous to Environmental Degradation of High-strength Steels, ISIJ International 43 (2003) 520–526.